

1 **Investigation of non-linear wave-induced seabed response around mono-pile**  
2 **foundation**

3 Zaibin Lin<sup>a</sup>, Dubravka Pokrajac<sup>b</sup>, Yakun Guo<sup>c</sup>, Dong-sheng Jeng<sup>d</sup>, Tian Tang<sup>e</sup>, Nick Rey<sup>f</sup>,  
4 Jinhai Zheng<sup>g,h</sup>, Jisheng Zhang<sup>g,h</sup>

5 a. School of Engineering, University of Aberdeen, AB24 3UE, UK,

6 Corresponding author: zaibin.lin@gmail.com

7 b. School of Engineering, University of Aberdeen, AB24 3UE, UK

8 c. School of Engineering, University of Bradford, BD7 1DP, UK,

9 d. Griffith School of Engineering, Griffith University Gold Coast Campus, Queensland  
10 4222, Australia

11 e. Bekaert Technology Center, Bekaert Company, Zwevegem, Belgium

12 f. Wood Group Kenny, Aberdeen, UK

13 g. College of Harbour, Coastal and Offshore Engineering, Hohai University, Nanjing  
14 210098, China

15 h. Key Laboratory of Coastal Disaster and Defence (Hohai University), Ministry of  
16 Education, Nanjing 210098, China

17

18 **Abstract:** Stability and safety of offshore wind turbines with mono-pile foundations,  
19 affected by non-linear wave effect and dynamic seabed response, are the primary  
20 concerns in offshore foundation design. In order to address these problems, the effects  
21 of wave non-linearity on dynamic seabed response in the vicinity of mono-pile  
22 foundation is investigated using an integrated model, developed using OpenFOAM,  
23 which incorporates both wave model (waves2Foam) and Biot’s poro-elastic model. The  
24 present model was validated against several laboratory experiments and promising  
25 agreements were obtained. Special attention was paid to the systematic analysis of pore  
26 water pressure as well as the momentary liquefaction in the proximity of mono-pile  
27 induced by nonlinear wave effects. Various embedded depths of mono-pile relevant for  
28 practical engineering design were studied in order to attain the insights into nonlinear

29 wave effect around and underneath the mono-pile foundation. By comparing time-series  
30 of water surface elevation, inline force, and wave-induced pore water pressure at the  
31 front, lateral, and lee side of mono-pile, the distinct nonlinear wave effect on pore water  
32 pressure was shown. Simulated results confirmed that the presence of mono-pile  
33 foundation in a porous seabed had evident blocking effect on the vertical and horizontal  
34 development of pore water pressure. Increasing embedded depth enhances the blockage  
35 of vertical pore pressure development and hence results in somewhat reduced momentary  
36 liquefaction depth of the soil around mono-pile foundation.

37

38 **Key words:** wave-structure-seabed interaction (WSSI); dynamic seabed response; mono-  
39 pile foundation; blockage effect; momentary liquefaction

40

## 41 **1. Introduction**

42 Demand for green energy in response to climate change has driven a substantial increase of  
43 construction of offshore wind farms in the past decades, which is likely to continue in the  
44 forthcoming years. Large diameter mono-pile is the preferred foundation for offshore wind  
45 turbines located in shallow or intermediate water depths. Mono-pile foundation supporting  
46 offshore wind turbine may suffer the damage from strongly non-linear, and even breaking  
47 waves. The soil near a mono-pile foundation may be liquefied under wave loading and in  
48 turn aggravate the vibration of the offshore wind turbine. Understanding these mechanisms  
49 and accurate prediction of their influences on mono-pile foundations are therefore  
50 particularly important in engineering design.

51

52 In recent decades, wave-induced hydrodynamic loads acting on the cylindrical structure have  
53 been extensively studied since they are of primary concern in offshore engineering. The  
54 costly and time-consuming laboratory experiments cannot provide a complete set of results  
55 on wave-structure interaction. Consequently, the numerical models of wave-structure  
56 interaction have been increasingly used. Based on potential theory and the assumption that  
57 flow is inviscid and irrotational, various numerical analyses of linear and weakly non-linear

58 wave-structure interactions have been presented. To study the three-dimensional (3-D)  
59 wave-structure interaction, Ma et al. (2001a, 2001b) numerically solved the fully non-linear  
60 potential flow with Finite Element Method (FEM) incorporating recovery technique to  
61 obtain better solution. The same approach was used by Kim et al. (2006) to investigate wave  
62 run-up around cylinders with steeper Stokes waves. The technique of domain decomposition  
63 with enforcing continuity of the interface between neighbour subdomains was implemented  
64 by Bai and Taylor (2007, 2009) to examine fully nonlinear wave interaction with vertical  
65 cylinder. However, the potential flow theory is limited to non-breaking and small steepness  
66 waves (small  $H/L_w$ , where  $H$  is the wave height, and  $L_w$  is the wave length). The alternative  
67 that is becoming increasingly popular is to use Computational Fluid Dynamics (CFD) for  
68 investigating high steepness wave interacting with offshore structures, including breaking  
69 wave effect and higher-order harmonic forces. Recent CFD computations within the  
70 framework of OpenFOAM based on Finite Volume Method (FVM), a free access source  
71 C++ library for various fluid flow and solid mechanics problems, have been performed to  
72 obtain the insights into fully nonlinear wave-structure interactions. Using the wave  
73 generation tool waves2Foam (Jacobsen et al., 2012), Paulsen et al. (2014b) investigated the  
74 capacity of OpenFOAM for modelling nonlinear wave motion interacting with mono-pile  
75 foundation for a range of Keulegan–Carpenter ( $KC$ ) numbers,  $KC = U_m T/D$ , where  $U_m$  is  
76 the maximum velocity,  $T$  is wave period and  $D$  is the diameter of cylinder (Sumer and  
77 Fredsøe, 2006), and concluded that the dominant physics of wave-pile interactions was well  
78 predicted, despite the simplification of cylinder wall and the seabed surface boundary  
79 conditions. Paulsen et al. (2014a) introduced an innovative domain decomposition approach  
80 to integrate potential flow theory model (OceanWave3D) developed by Engsig-Karup et al.  
81 (2009) and waves2Foam library (Jacobsen et al., 2012) based on Navier-Stokes (NS)  
82 equations and volume of fluid method (VOF). Good agreement between numerical and  
83 experimental results has been obtained for several sensitivity tests of wave loads on a  
84 cylindrical pile foundation. A comprehensive investigation of the potential of OpenFOAM  
85 for accurately predicting the interactions between wave and vertical cylinder was elaborated  
86 by Chen et al. (2014) for a variety of wave conditions, including regular and focused waves.

87 Higuera et al. (2013a) developed an advanced wave generation tool and the active wave  
88 absorption boundary condition (IHFOAM) for predicting wave interaction with coastal  
89 structures in coastal engineering (Higuera et al., 2013b; Higuera et al., 2014a; Higuera et al.,  
90 2014b). A moving boundary condition with multi-paddles for wave generation is further  
91 incorporated into IHFOAM (Higuera et al., 2015) together with an improved active wave  
92 absorption boundary. Nevertheless, the research solely concerning the mechanism of wave  
93 interacting with offshore structure does not fully cover the complexity of realistic design  
94 issues.

95

96 Another important issue in offshore engineering is the risk associated with formation of  
97 liquefied zone of seabed as a consequence of wave-induced dynamic seabed response in the  
98 vicinity of offshore structures (Sumer, 2014; Sumer and Fredsøe, 2002; Ye et al., 2015; Ye  
99 et al., 2016). Liquefaction can be caused by two different mechanisms which occur at  
100 different time-scales, so we distinguish between residual and momentary liquefaction.  
101 Residual liquefaction typically occurs in un-drained soils, when the pore water pressure  
102 accumulated over time exceeds overburden pressure (Sumer, 2014). A much shorter-lived  
103 phenomenon, termed momentary liquefaction, occurs in an unsaturated seabed, due to the  
104 direct effect of wave pressure imposed on seabed surface under wave trough. The resulting  
105 fast decrease of pore water pressure in the unsaturated seabed generates large upwards  
106 pressure gradients. If the lift induced by upward gradient of pore water pressure surpasses  
107 the submerged weight of soil, effective stress vanishes and the soil is liquefied. From  
108 geotechnical aspect, the occurrence of liquefaction under extreme wave impact during storm  
109 conditions may result in the failure of the supporting foundation of an offshore structure, as  
110 well as foundation protection. The relationship between momentary liquefaction and  
111 extreme wave interaction with mono-pile foundation is the primary focus of present study.

112

113 In past decades, the analytical studies of wave-induced seabed response have also been  
114 extensively carried out. Madsen (1978) and Yamamoto et al. (1978) extended the poro-  
115 elastic Biot's theory (Biot, 1941) to a close-form analytical solution for the examination of

116 wave-induced seabed response. Afterwards the investigation of wave-induced response for  
117 both coarse and fine sand, using a boundary-layer approximation, was conducted by Mei and  
118 Foda (1981). They pointed out that their approach can be used to economically solve poro-  
119 elastic boundary value problem with a free surface. Using plane stress conditions, Okusa  
120 (1985) studied wave-induced stability of completely or partially saturated seabed with a  
121 conclusion that Skempton's pore pressure coefficient played a key role in predicting wave-  
122 induced seabed response. Hsu and Jeng (1994) analytically derived a closed-form solution  
123 to investigate short-crested wave-induced soil response within the case of a finite thickness  
124 seabed. A good agreement was found between their results and semi-analytical solution  
125 (Yamamoto et al., 1978). After then, a thorough review on research of wave-induced  
126 dynamic seabed response was described by Jeng (2003), where both theoretical and physical  
127 studies are included and examined in detail. Most recently, with the fully dynamic soil  
128 behaviour considered, Liao et al. (2013) presented an analytical study of combined effect of  
129 wave and current over an infinite seabed. It was noted that the effect of currents on the seabed  
130 response was significant only in the upper area closed to seabed surface (about 10% of wave  
131 length). Nevertheless, the aforementioned analytical investigations are limited to given  
132 assumptions and scenarios.

133

134 To improve understanding of the entire wave-induced seabed response multiple physical  
135 experiments were conducted with/without structures. Based on the laboratory experiments  
136 in a wave flume, Sumer et al. (2006) elaborated the mechanism of wave-induced liquefaction  
137 and consecutive compaction of a flat seabed without structures, and suggested that the  
138 completion of compaction and final equilibrium with continuing waves produces ripples.  
139 The laboratory experiments of Sumer et al. (2007) confirmed that when the progressive wave  
140 was greater than critical wave height, the soil around a pile, that was freshly settled without  
141 liquefaction history, may experience liquefaction after installation. In the dense-silt scour  
142 tests, it was also demonstrated that the scour around the pile may occur after liquefaction  
143 and compaction. Liu et al. (2015) conducted one-dimensional (1-D) soil column experiments  
144 to investigate wave-induced pore water pressure in various sandy soil conditions. The soil

145 thickness was found to decrease due to the dynamic loading. Though the realistic mechanism  
146 of wave-induced seabed response is easily captured by using natural materials, physical  
147 experiments are relatively expensive to carry out and restricted to the limited-scale cases.

148

149 Numerical modelling has been broadly employed as a cost-effective method for investigating  
150 seabed response induced by various wave conditions. Li et al. (2011) used FEM approach to  
151 numerically solve the 3-D Biot's equations without considering wave diffraction in their  
152 model. Wave-induced seabed response around pile foundation, including transient and  
153 residual pore water pressure, was examined for different pile diameters. However, in this  
154 study, the incident wave was simplified as an analytical solution, so that the complicated  
155 wave-structure interaction was not taken into consideration. The rapid development of  
156 computing resources enables researchers to couple flow model with seabed model into an  
157 integrated model, which enables them to systematically investigate the mechanisms of  
158 seabed response to waves in the vicinity of offshore structures, such as pipelines (Zhao et al.,  
159 2014; Lin et al., 2016; Zhao et al., 2016a; 2016b; 2016c) and breakwaters (Jeng et al., 2013;  
160 Jianhong et al., 2014; Jianhong et al., 2013; Ye et al., 2013a; 2013b). In the previous studies,  
161 the equations governing fluid and soil behaviour were solved by different methods, namely  
162 flow field by FVM and soil model by FEM. A monolithic approach to both models was used  
163 in Lin et al. (2016), who developed an integrated FEM Wave-Seabed-Structure Interaction  
164 (WSSI) model to explore the wave-induced liquefaction potential in the vicinity of a  
165 partially/fully buried pipeline in an open trench. As an alternative approach, Liu et al. (2007)  
166 first discretized the Biot's equations in a FVM manner within OpenFOAM, and then  
167 investigated the wave-induced response around the submerged object without parallel  
168 computing. Tang et al. (2015) and Tang (2014) extended and modified the poro-elastic Biot's  
169 model to poro-elasto-plastic soil model. However, so far majority of integrated models have  
170 focused on the investigation of wave-pipeline/breakwater-seabed interaction. For the wave-  
171 pile-seabed interaction, a numerical study based on FVM-FEM approach carried out by  
172 Chang and Jeng (2014) showed that replacing the soil around a high-rising structure  
173 foundation was an effective protection against liquefaction. The only available numerical

174 model of WSSI focuses solely on the dynamic seabed response induced by weakly nonlinear  
175 waves or regular non-breaking waves. Recently, Sui et al. (2015) integrated FUNWAVE  
176 (Kirby et al., 2003; Shi et al., 2001; Wei and Kirby, 1995) and fully dynamic (FD) form of  
177 Biot's equations to investigate the small steepness wave-induced seabed response around  
178 mono-pile without considering fully nonlinear wave-pile interaction. In their study, dynamic  
179 response of porous seabed, structural dynamics of mono-pile, and their interactions were all  
180 solved by FD form of Biot's equations. However, the non-linear wave-pile interaction has a  
181 significant effect on porous seabed response. This complex process is not fully studied in the  
182 aforementioned studies. Consequently, an integrated WSSI numerical model capable of  
183 accurately estimating strongly nonlinear wave load and the corresponding dynamic seabed  
184 response provides an efficient tool for the design of offshore wind turbine foundations.

185

186 This paper presents a sophisticated WSSI numerical model developed in order to aid the  
187 design for offshore wind turbine foundations. A segregated FVM solver is implemented  
188 within the framework of OpenFOAM, incorporating waves2Foam and Biot's equations, to  
189 address the issue of nonlinear wave-induced dynamic seabed response surrounding mono-  
190 pile foundation. The description of wave and seabed model is outlined in Section 2. Section  
191 3 presents the validation of present model against several available experimental data sets.  
192 In Section 4 the calibrated model is used to investigate the nonlinear wave-induced dynamic  
193 seabed response, as well as the liquefaction potential, around mono-pile foundation. The  
194 main conclusions are listed in Section 5.

195

## 196 **2. Numerical model**

197 Figure 1 shows a sketch of simulation domain for the WSSI numerical model developed in  
198 this study. The domain includes two sub-domains: the sea water (including the air above the  
199 free surface) and the porous bed. The two corresponding sub-models, namely waves2Foam  
200 (Jacobsen et al., 2012) and QS (quasi-static) Biot's model, are integrated into the present  
201 WSSI model. The flow field is described by the incompressible Navier-Stokes equations  
202 with water-air interface traced by Volume of Fluid method (Berberović et al., 2009; Hirt and

203 Nichols, 1981). The dynamic behaviour of a porous seabed is governed by QS Biot's  
 204 equations, which contain both the pore water pressure and soil displacement. The process of  
 205 integration is implemented by extended general grid interpolation (GGI), which interpolates  
 206 the face and point from zone to zone for non-conformal meshes at the wave-seabed interface  
 207 (Tukovic et al., 2014).

208

## 209 2.1 Wave model

210 The governing equations for simulating two-phase incompressible flow dynamics are

$$\nabla \cdot \mathbf{u} = 0 \quad (1)$$

$$\frac{\partial \rho \mathbf{u}}{\partial t} + \nabla \cdot (\rho \mathbf{u}) \mathbf{u}^T = -\nabla p^* - (\mathbf{g} \cdot \mathbf{x}) \nabla \rho + \nabla \cdot (\mu \nabla \mathbf{u}) \quad (2)$$

$$\frac{\partial \alpha}{\partial t} + \nabla \cdot \mathbf{u} \alpha + \nabla \cdot \mathbf{u}_r \alpha (1 - \alpha) = 0 \quad (3)$$

211 where  $\mathbf{u}$  is velocity field;  $\rho$  is fluid density;  $t$  is time;  $p^* = p - \rho \mathbf{g} \cdot \mathbf{x}$  is the modified  
 212 pressure which removes the effect of static pressure from the momentum equation (2);  $\mathbf{g}$   
 213 and  $\mathbf{x}$  are gravity acceleration and Cartesian coordinate vector, respectively;  $p$  is total  
 214 pressure;  $\mu$  is dynamic viscosity;  $\mathbf{u}_r$  is relative velocity field (Berberović et al., 2009);  $\alpha$   
 215 is scalar field of volume fraction function.  $\alpha$  is equivalent to 1 when the computational cell  
 216 indicates water field, while  $\alpha = 0$  indicates the simulated field to be air, and the water-air  
 217 mixture field is denoted by  $0 < \alpha < 1$ . The momentary flow density and dynamic viscosity  
 218 are computed by following equations:

$$\rho = \alpha \rho_w + \rho_a (1 - \alpha) \quad (4)$$

$$\mu = \alpha \mu_w + \mu_a (1 - \alpha) \quad (5)$$

219 where the sub-indices  $w$  and  $a$  represent water and air, respectively.

220

221 Consistently with the investigation by Paulsen et al. (2014b), where boundary layer effects  
 222 were not taken into consideration, slip boundary condition is specified on the seabed, mono-  
 223 pile surface, and lateral boundaries of the numerical wave flume. The atmospheric boundary  
 224 at the upper boundary of flow domain is selected as a pressure outlet condition. The more



225 comprehensive description of wave generation (inlet boundary) and wave absorption (outlet  
226 boundary) zone can be found in Jacobsen et al. (2012).

227

## 228 2.2 Seabed model

229 In present study, QS Biot's equations (Biot, 1941) are adopted as the governing equations  
230 for describing wave-induced dynamic soil response in a hydraulically isotropic porous  
231 seabed. The combined continuity and motion equation for the pore water is:

$$\nabla^2 p_p - \frac{\gamma_w n_s \beta_s}{k_s} \frac{\partial p_p}{\partial t} = \frac{\gamma_w}{k_s} \frac{\partial \varepsilon_s}{\partial t} \quad (6)$$

232 where  $p_p$  is wave-induced pore water pressure (i.e. pore water pressure in excess of the  
233 static pressure due to mean seawater level);  $\gamma_w$  is the unit weight of pore water;  $n_s$  is soil  
234 porosity;  $k_s$  is the Darcy's permeability assumed to be the same in all directions. The  
235 compressibility of pore fluid  $\beta_s$  and the volume strain  $\varepsilon_s$  are defined by

$$\beta_s = \frac{1}{K_w} + \frac{1 - S_r}{P_{w0}} \quad (7)$$

$$\varepsilon_s = \nabla \cdot \mathbf{v} = \frac{\partial u_s}{\partial x} + \frac{\partial v_s}{\partial y} + \frac{\partial w_s}{\partial z} \quad (8)$$

236 where  $K_w$  is the bulk modulus of pore water (adopted as  $2 \times 10^9$  N/m<sup>2</sup> in Section 3.2,  
237 Yamamoto et al., 1978, and  $2.3 \times 10^9$  N/m<sup>2</sup> in Section 4, Hansen, 2012);  $S_r$  is soil saturation  
238 degree;  $P_{w0}$  is absolute static water pressure;  $\mathbf{v} = (u_s, v_s, w_s)$  is soil displacement vector.  
239

240 The force equilibrium in a poro-elastic seabed can be calculated via following equation:

$$G \nabla^2 \mathbf{v} + \frac{G}{1 - 2\nu} \nabla \varepsilon_s = \nabla p_p \quad (9)$$

241 where  $G$  is the shear modulus of soil and can be obtained through Young's modulus ( $E$ ) and  
242 Poisson's ratio ( $\nu$ ):

$$G = \frac{E}{2(1 + \nu)} \quad (10)$$

243 Hansen (2012) suggested that Young's modulus ( $E$ ) for the soil at large depth within a seabed  
244 can be determined by

$$E = E_{ref} \left( \frac{\sigma'_3}{\sigma'_{3,ref}} \right)^\alpha \quad (11)$$

245 where  $E_{ref}$  is reference Young's modulus of soil,  $\sigma'_3$  and  $\sigma'_{3,ref}$  are confining pressure  
 246 and reference confining pressure, respectively,  $\alpha$  is a constant ranging from 0.5 to 0.7 for  
 247 sand.

248

249 In accordance with the generalized Hooke's law, effective normal stress,  $\sigma'_i$ , and shear  
 250 stress,  $\tau_{ij}$ , where the subscripts  $i,j=x,y,z$  indicate the direction of Cartesian coordinate, can  
 251 be determined by

$$\sigma'_x = 2G \left( \frac{\partial u_s}{\partial x} + \frac{\nu}{1-2\nu} \varepsilon_s \right), \sigma'_y = 2G \left( \frac{\partial v_s}{\partial y} + \frac{\nu}{1-2\nu} \varepsilon_s \right) \quad (12)$$

$$\sigma'_z = 2G \left( \frac{\partial w_s}{\partial z} + \frac{\nu}{1-2\nu} \varepsilon_s \right), \tau_{xy} = \tau_{yx} = G \left( \frac{\partial u_s}{\partial y} + \frac{\partial v_s}{\partial x} \right) \quad (13)$$

$$\tau_{xz} = \tau_{zx} = G \left( \frac{\partial u_s}{\partial z} + \frac{\partial w_s}{\partial x} \right), \tau_{yz} = \tau_{zy} = G \left( \frac{\partial v_s}{\partial z} + \frac{\partial w_s}{\partial y} \right) \quad (14)$$

252 Several boundary conditions have to be specified at the boundary of seabed domain and the  
 253 pile-seabed interface for an accurate prediction of WSSI. At seabed surface,  $y=0$  (Fig. 1), the  
 254 wave-induced pore water pressure,  $p_p$ , is set equal to  $p^*$  obtained from the wave model, and  
 255 vertical effective normal stress and shear stresses are considered to be 0,

$$\sigma'_z = \tau_{xy} = \tau_{yz} = 0, p_p = p^* \text{ at } y = 0 \quad (15)$$

256 At the bottom of seabed ( $y = -h_s$ , where  $h_s$  is soil depth, Fig. 1), an impermeable rigid  
 257 boundary condition is applied, where soil displacement is zero and there is no vertical flow:

$$u_s = v_s = w_s = \frac{\partial p_p}{\partial y} = 0 \text{ at } y = -h_s \quad (16)$$

258 The same no flow (zeroGradient) and zero soil displacement boundary condition is applied  
 259 at the lateral boundaries (Chang and Jeng, 2014):

$$u_s = v_s = w_s = \frac{\partial p_p}{\partial x} = 0 \text{ at } x = 0 \text{ and } x = L_s \quad (17)$$

$$u_s = v_s = w_s = 0, \frac{\partial p_p}{\partial z} = 0 \text{ at } z = -W_s/2 \text{ and } z = W_s/2 \quad (18)$$

260 In order to eliminate the influence of lateral boundaries, the length,  $L_s$ , and the width,  $W_s$ , of  
 261 simulation domain (Fig. 1), were taken as four times the wavelength,  $L_w$ , and sixteen times  
 262 the mono-pile diameter  $D$ . This domain size was used in Chen et al. (2014) to investigate  
 263 wave-structure interaction. It is reported in Ye and Jeng (2012) that the soil domain length  
 264 ( $L_s$ ) larger than double wavelength is sufficient to eliminate the impact from fixed lateral

265 boundaries. Thus, the mono-pile is located at the centre of computing domain and the lateral  
266 boundary of soil domain does not affect the simulated results around mono-pile foundation.  
267 Additionally, mono-pile is simulated as a rigid impermeable object so that at its surface the  
268 no-flow boundary condition applies, i.e. the gradient of pore water pressure vanishes:

$$\frac{\partial p_p}{\partial \mathbf{n}} = 0 \quad (19)$$

269 where  $\mathbf{n}$  denotes the normal to mono-pile surface. This boundary condition is acceptable for  
270 the rigid object located within a porous seabed (Chang and Jeng, 2014; Lin et al., 2016; Zhao  
271 et al., 2016a).

272

### 273 2.3 Integration process between wave and seabed model

274 Unlike the previous two-dimensional (2-D) monolithically integrated model in COMSOL  
275 Multiphysics using FEM (Lin et al., 2016), the three-dimensional (3-D) one-way integrated  
276 WSSI model is proposed in OpenFOAM with FVM. The present integrated model is able to  
277 simulate the wave-structure interaction more accurately, with low-cost of computer memory,  
278 and with high mesh density in the 3-D case. It solves the wave and soil model by two steps  
279 within one time step as illustrated in Fig. 2. First of all, in accordance with input wave  
280 parameters and the adjustable time step calculated by Courant–Friedrichs–Lewy (CFL)  
281 condition (adopted as 0.5 in this study), the wave model solves the Navier-Stokes and  
282 Volume of Fluid equations by the combined algorithm (PISO-SIMPLE, namely PIMPLE)  
283 for pressure-velocity coupling. Secondly, the dynamic wave pressure is extracted from wave  
284 model and applied to seabed surface through extended general grid interpolation (GGI)  
285 (Tukovic et al., 2014), which allows the integrated model to run WSSI computation in  
286 parallel within a time step compared to the serial WSSI simulation in Liu et al. (2007). The  
287 soil model then computes the wave-induced dynamic seabed response by solving QS Biot’s  
288 equations using FVM method (Tang and Hededal, 2014). After the completion of two sub-  
289 models simulations within a time step, the integrated model exports the simulated results  
290 based on pre-set writing time interval and then continues to the next time step simulation  
291 until the prescribed total simulation time is reached.

292

### 293 3. Validation

294 In this section, we validate both wave and seabed components of the integrated WSSI model  
295 against the available published laboratory experimental results. The lateral and plan views  
296 of numerical domains are shown in Fig. 1. The wave characteristics and soil properties used  
297 for validation are listed in Table 1.

298

#### 299 3.1. Wave model

300 Before applying the present WSSI to practical engineering, the ability of model to accurately  
301 simulate wave nonlinearity when interacting with a mono-pile needs to be investigated. The  
302 experimental data presented in Chen et al. (2014) and Zang et al. (2010) are adopted to  
303 validate present wave model. Two types of regular wave, one with the wave height  $H = 0.14$   
304 m, and the wave period  $T = 1.22$  s, and another one with  $H = 0.12$  m,  $T = 1.63$  s, are used to  
305 study the nonlinear wave-structure interaction. To reproduce the laboratory experiment a 3-  
306 D numerical wave tank was established, as shown in Fig. 1, but without seabed sub-domain.  
307 In laboratory experiment, the diameter of mono-pile,  $D$ , is 0.25 m, while mean water depth,  
308  $h_w$ , is 0.505 m. On the basis of the investigation of mesh sensitivity by Paulsen et al. (2014b),  
309 the refined mesh with a resolution of 15 points per wave height is adopted in the validation.

310

311 Fig. 1 also shows several wave gauges and pore water pressure sensors locations for model  
312 validations and further applications in the numerical wave-seabed tank. Wave gauge 1 at  
313 0.77 m from the inlet, and Wave gauge 2 at 0.002 m distance from the upstream mono-pile  
314 surface along the centreline are used to measure free surface elevation,  $\eta$ . Fig. 3 (a) shows  
315 the comparison of simulated and experimental free surface elevation for the incident wave,  
316 i.e. at Wave gauge 1. The simulated incident wave is in a good agreement with the  
317 experimental results. The time series of simulated and experimental free surface level close  
318 to the mono-pile (at Wave gauge 2) for two different regular waves are shown in Fig. 3(b)  
319 and 3(c). Excellent agreement between numerical and experimental results denote that  
320 present wave model has the capacity to simulate the strongly nonlinear behaviour of waves  
321 interacting with mono-pile, including the small jump after wave troughs.

322

323 The simulated wave-induced inline force on the surface of mono-pile,  $F_x$ , is also compared  
324 with experimental results in Fig. 4. The simulated inline force is calculated by spatial  
325 integration of the total pressure,  $p$ , over the surface of the mono-pile exposed to sea water  
326 (the water sub-domain in Fig. 1). Despite minor discrepancy at wave nodes the agreement  
327 between computed and experimental results is generally good, hence showing that the  
328 application of present wave model to practical engineering is promising. The aforementioned  
329 validations show that nonlinearity of wave-pile interaction is accurately predicted in the  
330 numerical wave tank in both cases. It can be concluded that present wave model  
331 (waves2Foam) is capable of capturing the nonlinear wave-pile interactions, including free  
332 surface elevation and wave load on the mono-pile.

333

### 334 3.2. Wave-seabed interaction model

335 Wave-induced dynamic seabed response was validated by comparison of simulation results  
336 with the laboratory experiment of Liu et al. (2015). The laboratory experiment was carried  
337 out in a one-dimensional column filled with sand saturated with water, and exposed to a  
338 periodic variation of pressure at the cylinder top. The time series of the resulting variation  
339 of pore water pressures was measured at several locations along the column. The soil  
340 properties used for validation are listed in Table 1 and the reader is referred to Liu et al.  
341 (2015) for more details. In order to eliminate the potential effect from lateral boundaries, the  
342 soil domain for validating soil model is designed as a 2-D case, in which the lateral and  
343 bottom boundary conditions are selected as demonstrated in section 2.2, and at seabed  
344 surface, analytical wave pressure based on laboratory experiment is imposed. The soil  
345 properties tabulated in Table 1 are measured in Liu et al. (2015), and then used as input  
346 parameters in the validation of soil model.

347

348 Vertical distribution of wave-induced pore water pressure from the experiment shown in Liu  
349 et al. (2015) is compared with numerical simulation in Fig. 5. Results are scaled with the  
350 maximum pore water pressure at seabed surface,  $P_0$ . The simulated results generally agree

351 with the experiment and the analytical result (Hsu and Jeng, 1994) except for an obvious  
352 discrepancy at the position close to seabed bottom ( $y/h_s=-0.8$ ). A possible explanation, given  
353 in Liu et al. (2015), is that the soil in the physical test was not perfectly homogeneous, i.e.  
354 soil properties could have been different close to the bottom, while in numerical model soil  
355 properties are constant. The time series of wave-induced pore water pressure at the depth  $y$   
356  $= -0.067$  m ( $y/h_s=-0.037$ ) against experimental data is shown in Fig. 6, in which  $\omega$  is wave  
357 frequency. The numerical prediction agrees well with the experimental results. In conclusion  
358 we are confident that the present seabed model in OpenFOAM has the capacity to accurately  
359 model the wave-induced dynamic seabed response.

360

#### 361 **4. Application**

362 In reality, the foundations of offshore mono-piles are protected by granular filters in order to  
363 prevent scour which may result in the failure of the offshore structures. As pointed out by  
364 Kirca (2013), the seabed beneath granular filters may experience liquefaction in the seabed  
365 below. Following the satisfactory validations present coupled WSSI model is further applied  
366 to investigate dynamic seabed response in the proximity of mono-pile foundation due to  
367 nonlinear effect of wave-pile interaction at intermediate water depth. In this example, the  
368 wave from the Danish ‘Wave loads’ project (Paulsen et al., 2014b) is considered, and the  
369 wave field interacts with a mono-pile of 6 m diameter ( $D$ ). The mean water depth is constant,  
370  $h_w = 20$  m. The detailed wave and seabed parameters for investigation of nonlinear wave-  
371 induced seabed response around mono-pile are listed in Table 2. To determine the  
372 distribution of Young’s modulus ( $E$ ) in seabed,  $E_{ref} = 177$  MPa,  $\sigma'_{3,ref} = 150$  kPa, and  $\alpha$   
373  $= 0.62$  are used in accordance with the medium sand in Eskesen et al. (2010). In reality the  
374 vibration of mono-pile due to the action of violent wave may compact granular soil and urge  
375 the air out, leading to a denser and more saturated soil around mono-pile foundation during  
376 pile vibration. In present study this phenomenon is not simulated, mono-pile is assumed to  
377 be very rigid and the seabed saturation is adopted as a constant (Table 2). The focus of  
378 present study is therefore solely on dynamic behaviour of porous seabed and associated  
379 potential liquefaction around mono-pile foundation caused by the interaction of extreme

380 wave and mono-pile foundation.

381

382 The initial investigation is performed for a mono-pile that is embedded into seabed until the  
383 depth equal triple pile diameter. We first examine the connection between nonlinear wave  
384 and dynamic seabed response due to the blockage effect of mono-pile. According to the  
385 available momentary liquefaction criterion, the potential momentary liquefaction zone  
386 around mono-pile is studied in detail. The final part of this study investigates the influence  
387 of the embedment depth of mono-pile foundation, ranging from three to seven times pile  
388 diameter, on the dynamic seabed response to the action of high steepness waves.

389

390 4.1 Vertical distribution of pore water pressure in the vicinity of mono-pile

391 The vertical distribution of pore water pressure around pile is recorded at a series of vertical  
392 profiles located 0.05 m away from the surface of mono-pile with  $\theta$  ranging from  $0^\circ$  to  $180^\circ$   
393 with  $45^\circ$  increment (wave gauges 2-6 in Fig. 1), and at position 7 located in the centre of  
394 mono-pile. The corresponding vertical profiles of pore water pressures are shown in Fig. 7  
395 with  $t/T$  varying from 5.04 to 6.07, i.e. over one period. In general, the vertical distribution  
396 of pore water pressure has the greatest amplitudes at front face of mono-pile foundation,  $\theta =$   
397  $0^\circ$ , and the smallest amplitudes at  $\theta = 90^\circ$ . Between  $\theta=0^\circ$  and  $\theta=90^\circ$ , the overall pore water  
398 pressures along embedment depth reduce, while beneath the pile there is only a slight  
399 decrease. For  $\theta$  between  $90^\circ$  and  $180^\circ$ , the trend reverses, resulting in peak pressures at  $\theta$   
400  $=180^\circ$ . The reason for these trends may be a consequence of free surface elevation variation  
401 together with the variation of wave pressure around mono-pile. The comparison and analysis  
402 of relationship between wave-pile interaction and pore water pressure distribution are  
403 elaborated in next section.

404

405 As shown by Zhang et al. (2015), the presence of mono-pile in seabed increases the pore  
406 water pressure along mono-pile foundation compared to that without mono-pile foundation  
407 penetrated into seabed. Fig. 7(a)-(e) shows that the magnitude of pore water pressure  
408 declines rapidly from the seabed surface to approximately  $y = -1.8$  m, and then slightly

409 decreases until the depth of about  $y = -17.46$  m, close to the pile bottom. Between  $y = -17.46$   
410 m and  $y = -19$  m, an evident fall of pore water pressure magnitude can be noticed. The  
411 explanation of this is that the soil below pile bottom may be shielded from the pore water  
412 pressure induced by propagating wave above. Fig. 7 (f) presents the pore water pressure  
413 along the central line of mono-pile bottom. In comparison with the pore water pressure  
414 around mono-pile circumference at  $y = -18$  m, the pore water pressure underneath pile  
415 bottom is relatively small and has limited variation. The limited impact of the wave pressure  
416 on the dynamic soil response under pile bottom at different  $\theta$ -locations also confirms the  
417 shielding effect of pile foundation.

418

#### 419 4.2 Wave-induced seabed response around mono-pile

420 The wave model validation has shown (Fig. 3) that high steepness wave has an evident  
421 nonlinearity when interacting with mono-pile. Wave crest and wave trough, as well as pore  
422 water pressure, develop nonlinearly due to interaction with mono-pile, compared to the case  
423 without mono-pile. This is primarily due to the blockage effect of mono-pile in the wave and  
424 pore water pressure propagating direction.

425

426 In order to further examine the notable variation of pressure at several vertical locations,  $y =$   
427 0 m, -1.8 m, -17.46 m, and -18 m, the time histories of pore water pressure at these locations,  
428 as well as the time history of free surface elevation are presented in Fig. 8, at the same  
429 locations 0.05 m away from mono-pile surface (wave gauges 2-6 in Fig. 1). The  $t/T$  from 4  
430 to 7, when the interaction of wave and mono-pile has attained the dynamic equilibrium, is  
431 considered. It can be noticed that the interaction between wave and mono-pile produces  
432 strong nonlinearity of free surface elevation, even wave-breaking at WG4 and WG5. This in  
433 turn affects pore water pressure, which shows similar albeit development history. By  
434 comparing free surface elevation at various wave gauges, it is implied that the maximum  
435 free surface elevation declines gradually with  $\theta$  increasing from  $0^\circ$  to  $135^\circ$  and, at WG6 ( $\theta$   
436 =  $180^\circ$ ), the maximum free surface elevation raises due to the merge of incident wave crest  
437 propagated separately from both lateral sides of pile (Swan and Sheikh, 2015). Pore water



438 pressure presents similar decrease when  $\theta$  grows from  $0^\circ$  to  $90^\circ$ , but different development  
439 at  $\theta = 135^\circ$ . It can be inferred that, when the free surface elevation is changing rapidly, the  
440 water pressure at the seabed, and hence also pore water pressure within the bed, do not  
441 respond simultaneously. The precise simulation of wave pressures around the pile is  
442 therefore required in order to accurately model the dynamic seabed response.

443

444 The second column of Fig. 8, shows that, while pore water pressure at  $y = -1.8$  m still shows  
445 similar development history as that at seabed surface, the effect of wave-pile interaction on  
446 pore water pressure becomes weaker as the observation point moves from  $-1.8$  m to  $-18$  m.  
447 The comparison of maximum pore water pressure at different  $\theta$  in Fig. 8 shows once more  
448 that the pore water pressure at  $\theta = 90^\circ$  reaches its minimum.

449

#### 450 4.3 Wave-induced liquefaction around pile

451 Liquefaction around offshore structures is considered as one of the primary threats to  
452 operational lifetime of these structures (Sumer, 2014), so it is a major concern in the  
453 engineering practice. Based on the liquefaction criterion suggested in Jeng (2013) and Sumer  
454 (2014), the potential liquefaction zone can be determined by

$$-(\gamma_s - \gamma_w)y \leq (p_{ps} - P_b) \quad (20)$$

455 where  $\gamma_s$  and  $\gamma_w$  are the unit weight of seabed and water, respectively ( $\gamma_s = 1.9 \gamma_w$  was  
456 used in this study);  $P_b$  is the pore water pressure on the seabed surface;  $p_{ps}$  is the pore  
457 water pressure within porous seabed. Liquefaction may occur in a porous seabed when the  
458 net excessive pore water pressure, equals to the difference between the pressure at seabed  
459 surface and pressure at a point beneath the surface, surpasses overburden soil pressure and  
460 soil matrix begins to lose its capacity for undertaking any load.

461

462 Using the aforementioned liquefaction criterion, maximum liquefied depth was evaluated  
463 and its time series is shown in Fig. 9, along with free surface elevation and inline force.  
464 Comparison between Fig. 9 (a) and (c) shows that the momentary liquefaction close to mono-  
465 pile surface takes place periodically at the moment when free surface elevation at WG2 is

466 smaller than 0 and inline force has its minimum (see Fig. 9). As a consequence of the  
467 propagation of wave trough, liquefied depth reaches its maximum. Maximum liquefaction  
468 depth drops and disappears due to the arrival of wave crest and rapid increase of free surface  
469 elevation and excess pressure on seabed surface from negative to positive, which in turn  
470 leads to decrease of the difference of pore water pressure at seabed surface and within seabed,  
471 which can be observed at  $t/T = 5.33$  to  $5.92$  in Fig. 7.

472

473 Comparison of Fig. 9 (b) and (c) in the case with  $KC$  number being 8.85 and  $D/L$  being 0.032,  
474 shows that during the potential liquefaction period, very close to maximum depth, there is  
475 also negative inline force directed upstream ( $F_x < 0$ ). As a result of this, the liquefied soil in  
476 the closest vicinity of mono-pile loses its support and then may enlarge mono-pile vibration,  
477 which is induced by periodic inline force. As mentioned earlier this periodic vibration of  
478 mono-pile foundation may pressurize adjacent soil in the vibration direction, and force the  
479 air out. As a consequence this process tend to harden surrounding soil and alter soil  
480 properties. For pile-seabed interaction, the reader is referred to Hansen (2012) for more  
481 details. To avoid the threat from potential liquefaction around foundation, Chang and Jeng  
482 (2014) suggested that momentary liquefaction may be prevented by replacing the existing  
483 soil layer with coarse sand layer with greater permeability.

484

485 Further presentation of the extent of liquefaction potential is shown in Fig. 10 at  $t/T = 5.66$ ,  
486 when liquefaction depth is the largest (highlighted by black hollow circle in Fig. 9 (c)). As  
487 shown in Fig. 10 (a) and (b), momentary liquefaction potential arises broadly while wave  
488 trough is approaching mono-pile over porous seabed. Compared with the liquefaction zone  
489 without mono-pile in the far field, liquefaction at front and back face of mono-pile  
490 foundation are relatively smaller. Fig. 10 (c) shows the liquefaction depth at the interface  
491 between soil and foundation with  $\theta$  ranging from  $0^\circ$  to  $180^\circ$ . The liquefaction depth is about  
492 1 m at the front face of pile foundation; it gradually increases as the observation point moves  
493 around the pile perimeter to reach maximum of approximately 1.5 m at  $\theta = 90^\circ$ , and then  
494 slightly reduces as the point moves from  $\theta = 90^\circ$  and  $\theta = 180^\circ$ . The temporal evolution of

495 the liquefaction depth at several  $\theta$ -locations along the pile perimeter are presented in Fig. 10  
496 (d). The liquefaction first appears at front face of mono-pile foundation and then rapidly  
497 approaches its lateral side ( $\theta = 90^\circ$ ), where the maximum liquefaction depth occurs. Between  
498 the lateral side and the back face there is further slight delay and slight decrease of the  
499 maximum liquefaction depth.

500

501 Momentary liquefaction in porous seabed propagates along with the wave trough above  
502 seabed. For the purpose of investigating possible threat from momentary liquefaction to  
503 scour protection, maximum potential liquefaction depth in the vicinity of mono-pile  
504 foundation over a wave period ( $t/T$  from 5 to 6) is presented in Fig. 11. It can be observed  
505 that maximum liquefaction depth of around 1.5m is located in the lateral zone near mono-  
506 pile foundation, with  $\theta$  approximately ranging from  $60^\circ$  to  $110^\circ$ , while minimum potential  
507 liquefaction depth of approximately 1 m occurs at front and back side of mono-pile  
508 foundation, where  $\theta$  equals  $0^\circ$  and  $180^\circ$ , respectively. It can be inferred that for  $KC = 8.85$   
509 and  $D/L = 0.032$  the scour protection may experience greater liquefaction threat, which may  
510 cause it to sink, in the areas close to lateral sides of mono-pile foundation than in the areas  
511 close to the front and back side.

512

#### 513 4.4 Influence of embedded depth

514 In reality, the ratios of embedded depth for mono-pile foundation of offshore wind turbine  
515 and mono-pile diameter often vary from 4 to 8 at shallow/intermediate water depth (Lesny  
516 et al., 2007). Therefore, for the same wave conditions listed in Table 2, the present model is  
517 further applied to the examples with two additional embedment depths, namely 30 m and 42  
518 m (Table 2), in order to investigate the effects of embedment depth on the development of  
519 pore water pressure and potential liquefaction.

520

521 Figures 12 and 13 show the development of vertical distribution of pore water pressure for  
522 the embedment depth of 30 m and 42 m respectively. For both cases the development of pore  
523 water pressure along embedment depth, as well as along pile bottom are similar to those

524 already shown in Fig. 7 (section 4.1), for the main case with the embedment depth of 18m.  
525 The development of the vertical pressure profiles around the pile perimeter is also similar  
526 for the three cases: pore water pressure declines as  $\theta$  grows from  $0^\circ$  to  $90^\circ$  and then raises  
527 with  $\theta$  ranging from  $90^\circ$  to  $180^\circ$ . However, the magnitude of pore water pressure along the  
528 foundation reduces as the embedment depth grows.

529

530 The estimated liquefaction depths in the aforementioned examples with 3 various penetration  
531 depths are shown in Fig. 14. At the front face of mono-pile foundation, the embedded depth  
532 has minor effect on liquefaction depth. The effect gradually increases as  $\theta$  grows from  
533 approximately  $30^\circ$  to  $180^\circ$ : increasing embedded depth results in smaller liquefaction depth.  
534 It can be inferred that increasing embedded depth has blocking effect on the pore water  
535 pressure propagation from front face to back face of mono-pile foundation. As a result, the  
536 pore water pressure along the mono-pile foundation with greater embedment depth presents  
537 slower reduction compared to that with smaller embedded depth, which eventually decreases  
538 the difference of pore water pressure along the embedded depth and leads to smaller  
539 liquefaction depth as shown in Fig. 14.

540

## 541 **5. Conclusions**

542 The numerical investigation of nonlinear wave-induced dynamic seabed response in the  
543 proximity of mono-pile foundation has been performed in detail using one-way coupled  
544 solver in OpenFOAM. In order to accurately describe the nonlinear wave interaction with  
545 mono-pile waves2Foam (Jacobsen et al., 2012) is applied for the numerical simulation of  
546 flow field. In soil model, the quasi-static Biot equations, solved by Finite Volume Method  
547 (Liu et al., 2007; Tang et al., 2015), govern the dynamic response of porous seabed around  
548 mono-pile foundation. A coupled scheme, based on extended general grid interpolation (GGI)  
549 (Tukovic et al., 2014) which allows the integrated model to run in parallel, is used to integrate  
550 both sub-models. The comparisons with available laboratory experimental results in the  
551 literature show excellent agreement for both wave and soil model. It demonstrates that this

552 integrated WSSI model is capable of estimating nonlinear wave-induced mechanical  
553 behaviour of poro-elastic seabed around offshore mono-pile-supported structure.

554

555 The benefits of the present model compared to those so far presented in the literature are: (1)  
556 nonlinear interaction of wave and mono-pile, including free surface elevation and inline  
557 force, is predicted accurately; (2) the resulting wave-induced dynamic seabed behaviour near  
558 mono-pile foundation is simulated simultaneously; (3) the associated momentary  
559 liquefaction potential in the vicinity of mono-pile foundation can also be estimated based on  
560 available liquefaction criteria. The model at present does not incorporate poro-elasto-plastic  
561 soil model, nor the interaction between mono-pile foundation and seabed. These two  
562 mechanisms, which may result in different impacts on seabed response, also play vital roles  
563 in the assessment of offshore foundation stability and will be integrated into the future model.

564

565 The following conclusions are drawn from the present study:

566 (1) The wave-induced pore water pressure is weakened as soil depth increases. The presence  
567 of mono-pile foundation leads to the noticeably different distribution of pore water  
568 pressure in the vicinity of foundation. The vertical distribution of pore water pressure  
569 around mono-pile foundation varies significantly with  $\theta$ : within a wave period, the range  
570 of pore water pressure reduces substantially between  $\theta = 0^\circ$  and  $\theta = 90^\circ$ , and then  
571 gradually increases as  $\theta$  grows from  $90^\circ$  to  $180^\circ$ . The range of pore water pressure at  $\theta$   
572  $= 90^\circ$  is the largest due to wave diffraction around mono-pile.

573

574 (2) Since pore water pressure within the seabed are attenuated compared to the pressures at  
575 seabed surface, the pressure difference between them generates an upward force resulting  
576 in the momentary liquefaction around mono-pile foundation. Application of a momentary  
577 liquefaction criterion shows that the horizontal distribution of liquefaction potential  
578 around mono-pile foundation (i.e. its variation with  $\theta$ ) is influenced by wave-pile  
579 interaction. Under the action of unidirectional regular waves with  $KC = 8.85$  and  $D/L =$   
580  $0.032$ , the maximum and minimum liquefaction depth take place at approximately  $\theta = 90^\circ$

581 and  $\theta = 180^\circ$ , respectively. In a wave period, maximum liquefaction depth occurs at the  
582 positions with  $\theta$  varying from  $60^\circ$  to  $110^\circ$ , where the scour protection may experience  
583 greater sinking compared to that at front and back sides of mono-pile foundation.  
584 However, since only one wave condition is taken into consideration, more investigations  
585 regarding various wave conditions are suggested to fully understand potential liquefaction  
586 around mono-pile foundation.

587

588 (3) Increasing embedded depth of mono-pile foundation significantly reduces the magnitude  
589 of pore water pressure along the embedded foundation, whereas the overall shape of the  
590 vertical pressure profiles remains similar. The increased blockage effect of larger  
591 embedded depths slightly reduces the difference of pore water pressure between the  
592 seabed and its surface, and hence also the corresponding liquefaction depth in the vicinity  
593 of the embedded mono-pile foundation.

594

### 595 **Acknowledgements**

596 The authors would like to acknowledge the financial support from Energy Technology  
597 Partnership (ETP), Wood Group Kenny, and University of Aberdeen. JH Zheng and JS  
598 Zhang would like to acknowledge the financial support from the National Science Fund for  
599 Distinguished Young Scholars (51425901) and the 111 project (B12032). The comments and  
600 suggestions provided by the anonymous Reviewers have greatly improved the quality of the  
601 final manuscript.

602

### 603 **References**

- 604 Bai, W., Taylor, R.E., 2007. Numerical simulation of fully nonlinear regular and focused  
605 wave diffraction around a vertical cylinder using domain decomposition. *Applied*  
606 *Ocean Research*, 29(1): 55-71.
- 607 Bai, W., Taylor, R.E., 2009. Fully nonlinear simulation of wave interaction with fixed and  
608 floating flared structures. *Ocean engineering*, 36(3): 223-236.
- 609 Berberović, E., van Hinsberg, N.P., Jakirlić, S., Roisman, I.V., Tropea, C., 2009. Drop impact

610 onto a liquid layer of finite thickness: Dynamics of the cavity evolution. *Physical*  
611 *Review E*, 79(3): 036306.

612 Biot, M.A., 1941. General theory of three - dimensional consolidation. *Journal of Applied*  
613 *Physics*, 12(2): 155-164.

614 Chang, K.-T., Jeng, D.-S., 2014. Numerical study for wave-induced seabed response around  
615 offshore wind turbine foundation in donghai offshore wind farm, shanghai, china.  
616 *Ocean Engineering*, 85: 32-43.

617 Chen, L., Zang, J., Hillis, A., Morgan, G., Plummer, A., 2014. Numerical investigation of  
618 wave–structure interaction using openfoam. *Ocean Engineering*, 88: 91-109.

619 Engsig-Karup, A.P., Bingham, H.B., Lindberg, O., 2009. An efficient flexible-order model  
620 for 3d nonlinear water waves. *Journal of computational physics*, 228(6): 2100-2118.

621 Eskesen, M., Buhrkall, J., Henningsen, J. (2010). 11761 - laboratoriepraktik. Technical  
622 report, Technical Universty of Denmark, Civil Engineering, Brovej, building 118,  
623 DK-2800 Kgs. Lyngby.

624 Hansen, NM, 2012. Interaction between Seabed Soil and Offshore Wind Turbine  
625 Foundations. Ph.D. thesis, Mechanical Engineering, Technical University of  
626 Denmark, Kgs. Lyngby, Denmark.

627 Higuera, P., Lara, J.L., Losada, I.J., 2013a. Realistic wave generation and active wave  
628 absorption for navier–stokes models: Application to openfoam®. *Coastal*  
629 *Engineering*, 71: 102-118.

630 Higuera, P., Lara, J.L., Losada, I.J., 2013b. Simulating coastal engineering processes with  
631 openfoam®. *Coastal Engineering*, 71: 119-134.

632 Higuera, P., Lara, J.L., Losada, I.J., 2014a. Three-dimensional interaction of waves and  
633 porous coastal structures using openfoam®. Part I: Formulation and validation.  
634 *Coastal Engineering*, 83: 243-258.

635 Higuera, P., Lara, J.L., Losada, I.J., 2014b. Three-dimensional interaction of waves and  
636 porous coastal structures using openfoam®. Part II : Application. *Coastal*  
637 *Engineering*, 83: 259-270.

638 Higuera, P., Losada, I.J., Lara, J.L., 2015. Three-dimensional numerical wave generation

639 with moving boundaries. *Coastal Engineering*, 101: 35-47.

640 Hirt, C.W., Nichols, B.D., 1981. Volume of fluid (vof) method for the dynamics of free  
641 boundaries. *Journal of computational physics*, 39(1): 201-225.

642 Hsu, J.R.C., Jeng, D.-S., 1994. Wave-induced soil response in an unsaturated anisotropic  
643 seabed of finite thickness. *International Journal for Numerical & Analytical Methods  
644 in Geomechanics*, 18(11): 785-807.

645 Jacobsen, N.G., Fuhrman, D.R., Fredsøe, J., 2012. A wave generation toolbox for the open -  
646 source cfd library: Openfoam®. *International Journal for Numerical Methods in  
647 Fluids*, 70(9): 1073-1088.

648 Jeng, D.-S., 2013. *Porous Models for Wave–Seabed Interactions*. Springer, Berlin  
649 Heidelberg, Germany.

650 Jeng, D.-S., 1997. Wave-induced seabed instability in front of a breakwater. *Ocean  
651 Engineering*, 24(10): 887-917.

652 Jeng, D.-S., 2003. Wave-induced sea floor dynamics. *Applied Mechanics Reviews*, 56(4):  
653 407-429.

654 Jeng, D.-S., Ye, J.H., Zhang, J.S., Liu, P.L.F., 2013. An integrated model for the wave-  
655 induced seabed response around marine structures: Model verifications and  
656 applications. *Coastal Engineering*, 72(0): 1-19.

657 Jianhong, Y., Dongsheng, J., Liu, P.L.F., Chan, A. H. C., Ren, W., Changqi, Z., 2014.  
658 Breaking wave-induced response of composite breakwater and liquefaction in seabed  
659 foundation. *Coastal Engineering*, 85: 72-86.

660 Jianhong, Y., Dongsheng, J., Ren, W., Changqi, Z., 2013. Numerical study of the stability of  
661 breakwater built on a sloped porous seabed under tsunami loading. *Applied  
662 Mathematical Modelling*, 37(23): 9575-9590.

663 Kim, J., Kyoung, J., Ertekin, R., Bai, K., 2006. Finite-element computation of wave-structure  
664 interaction between steep stokes waves and vertical cylinders. *Journal of waterway,  
665 port, coastal, and ocean engineering*, 132(5): 337-347.

666 Kirby, J., Wen, L., Shi, F., 2003. Funwave 2.0 fully nonlinear boussinesq wave model on  
667 curvilinear coordinates. Center for Applied Coastal Research Dept. of Civil &



668 Environmental Engineering, University of Delaware, Newark, USA.

669 Kirca, V.O., 2013. Sinking of irregular shape blocks into marine seabed under wave-induced  
670 liquefaction. *Coastal Engineering*, 75: 40-51.

671 Lesny, K., Paikowsky, S., Gurbuz, A., 2007. Scale effects in lateral load response of large  
672 diameter monopiles. *Geotechnical Special Publication*, 158: 1-10.

673 Li, X.-J., Gao, F.-P., Yang, B., Zang, J., 2011. Wave-induced pore pressure responses and  
674 soil liquefaction around pile foundation. *International Journal of Offshore and Polar  
675 Engineering*, 21(03):233–239

676 Liao, C., Jeng, D.-S., Zhang, L., 2013. An analytical approximation for dynamic soil  
677 response of a porous seabed due to combined wave and current loading. *Journal of  
678 Coastal Research*, 31(5): 1120-1128.

679 Lin, Z., Guo, Y., Jeng, D.-S., Liao, C., Rey, N., 2016. An integrated numerical model for  
680 wave–soil–pipeline interactions. *Coastal Engineering*, 108: 25-35.

681 Liu, B., Jeng, D.-S., Ye, G., Yang, B., 2015. Laboratory study for pore pressures in sandy  
682 deposit under wave loading. *Ocean Engineering*, 106: 207-219.

683 Liu, X., García, M.H., Muscari, R., 2007. Numerical investigation of seabed response under  
684 waves with free-surface water flow. *International Journal of Offshore and Polar  
685 Engineering*, 17(02).

686 Ma, Q., Wu, G., Eatock Taylor, R., 2001a. Finite element simulation of fully non - linear  
687 interaction between vertical cylinders and steep waves. Part 1: Methodology and  
688 numerical procedure. *International Journal for Numerical Methods in Fluids*, 36(3):  
689 265-285.

690 Ma, Q., Wu, G., Eatock Taylor, R., 2001b. Finite element simulations of fully non - linear  
691 interaction between vertical cylinders and steep waves. Part 2: Numerical results and  
692 validation. *International Journal for Numerical Methods in Fluids*, 36(3): 287-308.

693 Madsen, O.S., 1978. Wave-induced pore pressures and effective stresses in a porous bed.  
694 *Geotechnique*, 28(4): 377-393.

695 Mei, C.C., Foda, M.A., 1981. Wave-induced responses in a fluid-filled poro-elastic solid  
696 with a free surface—a boundary layer theory. *Geophysical Journal International*,

697           66(3): 597-631.

698   Okusa, S., 1985. Wave-induced stresses in unsaturated submarine sediments. *Geotechnique*,

699           35(4): 517-532.

700   Paulsen, B.T., Bredmose, H., Bingham, H.B., 2014a. An efficient domain decomposition

701           strategy for wave loads on surface piercing circular cylinders. *Coastal Engineering*,

702           86: 57-76.

703   Paulsen, B.T., Bredmose, H., Bingham, H.B., Jacobsen, N.G., 2014b. Forcing of a bottom-

704           mounted circular cylinder by steep regular water waves at finite depth. *Journal of*

705           *Fluid Mechanics*, 755: 1-34.

706   Qi, W.-G., Gao, F.-P., 2014. Physical modeling of local scour development around a large-

707           diameter monopile in combined waves and current. *Coastal Engineering*, 83: 72-81.

708   Shi, F., Dalrymple, R.A., Kirby, J.T., Chen, Q., Kennedy, A., 2001. A fully nonlinear

709           boussinesq model in generalized curvilinear coordinates. *Coastal Engineering*, 42(4):

710           337-358.

711   Sui, T., Zhang, C., Guo, Y., Zheng, J., Jeng, D.-S., Zhang, J., Zhang, W., 2015. Three-

712           dimensional numerical model for wave-induced seabed response around mono-pile.

713           *Ships and Offshore Structures*: 1-12.

714   Sumer, B.M., 2014. *Liquefaction Around Marine Structures*. World Scientific, New Jersey.

715   Sumer, B.M., Fredsøe, J., 2002. *The Mechanism of Scour in the Marine Environment*. World

716           Scientific, New Jersey.

717   Sumer, B.M., Fredsøe, J., 2006. *Hydrodynamics Around Cylindrical Structures*. World

718           Scientific, New Jersey.

719   Sumer, B.M., Hatipoglu, F., Fredsøe, J., 2007. Wave scour around a pile in sand, medium

720           dense, and dense silt. *Journal of waterway, port, coastal, and ocean engineering*,

721           133(1): 14-27.

722   Sumer, B.M., Hatipoglu, F., Fredsøe, J., Kaan Sumer, S., 2006. The sequence of sediment

723           behaviour during wave - induced liquefaction. *Sedimentology*, 53(3): 611-629.

724   Swan, C., Sheikh, R., 2015. The interaction between steep waves and a surface-piercing

725           column. *Philosophical Transactions of the Royal Society of London A: Mathematical*,

- 726 Physical and Engineering Sciences, 373(2033): 20140114.
- 727 Tang, T., 2014. Modeling of soil-water-structure interaction. A finite volume method (FVM)  
728 approach to fully coupled soil analysis and interactions between wave, seabed and  
729 offshore structure. Ph.D. thesis, Technical University of Denmark, Kgs. Lyngby,  
730 Denmark.
- 731 Tang, T., Hededal, O., 2014. Simulation of pore pressure accumulation under cyclic loading  
732 using Finite Volume Method. In Proceedings of 8th European Conference on  
733 Numerical Methods in Geotechnical Engineering (NUMGE14). Taylor & Francis.  
734 pp. 1301–1306
- 735 Tang, T., Hededal, O., Cardiff, P., 2015. On finite volume method implementation of poro-  
736 elasto-plasticity soil model. International Journal for Numerical and Analytical  
737 Methods in Geomechanics, 39(13): 1410-1430.
- 738 Tukovic, Z., Cardiff, P., Karac, A., Jasak, H., Ivankovic, A., 2014. Openfoam library for  
739 fluid structure interaction. 9th International OpenFOAM® Workshop, Zagreb,  
740 Croatia.
- 741 Wei, G., Kirby, J.T., 1995. Time-dependent numerical code for extended boussinesq  
742 equations. Journal of Waterway, Port, Coastal, and Ocean Engineering, 121(5): 251-  
743 261.
- 744 Yamamoto, T., Koning, H.L., Sellmeijer, H., Hijum, E.V., 1978. On the response of a poro-  
745 elastic bed to water waves. Journal of Fluid Mechanics, 87(01): 193-206.
- 746 Ye, J.-H., Jeng, D.-S., 2012. Response of porous seabed to nature loadings: waves and  
747 currents. Journal of Engineering Mechanics. ASCE 138, 601–613
- 748 Ye, J., Jeng, D.-S., Chan, A., Wang, R., Zhu, Q., 2016. 3D integrated numerical model for  
749 fluid–structures–seabed interaction (FSSI): Elastic dense seabed foundation. Ocean  
750 Engineering, 115: 107-122.
- 751 Ye, J., Jeng, D.-S., Wang, R., Zhu, C., 2013a. A 3-d semi-coupled numerical model for fluid–  
752 structures–seabed-interaction (FSSI-CAS 3D): Model and verification. Journal of  
753 Fluids and Structures, 40: 148-162.
- 754 Ye, J., Jeng, D.-S., Wang, R., Zhu, C., 2013b. Validation of a 2-d semi-coupled numerical

755 model for fluid–structure–seabed interaction. *Journal of Fluids and Structures*, 42:  
756 333-357.

757 Ye, J., Jeng, D.-S., Wang, R., Zhu, C., 2015. Numerical simulation of the wave-induced  
758 dynamic response of poro-elastoplastic seabed foundations and a composite  
759 breakwater. *Applied Mathematical Modelling*, 39(1): 322-347.

760 Zang, J., Taylor, P.H., Morgan, G.C.J., Orszaghova, J., Grice, J., Stringer, R., Tello, M., 2010.  
761 Steep wave and breaking wave impact on offshore wind turbine foundations–ringing  
762 re-visited. In *Proc. 25th International Workshop on Water Waves and Floating Bodies*,  
763 Harbin, China.

764 Zhang, C., Zhang, Q., Wu, Z., Zhang, J., Sui, T., Wen, Y., 2015. Numerical study on effects  
765 of the embedded monopile foundation on local wave-induced porous seabed  
766 response. *Mathematical Problems in Engineering*, 2015: 1.

767 Zhao, H.-Y., Jeng, D.-S., Liao, C., 2016a. Effects of cross-anisotropic soil behaviour on the  
768 wave-induced residual liquefaction in the vicinity of pipeline buried in elasto-plastic  
769 seabed foundations. *Soil Dynamics and Earthquake Engineering*, 80: 40-55.

770 Zhao, H.-Y., Jeng, D.-S., Liao, C., 2016b. Parametric study of the wave-induced residual  
771 liquefaction around an embedded pipeline. *Applied Ocean Research*, 55: 163-180.

772 Zhao, H.-Y., Jeng, D.-S., 2016c. Accumulation of pore pressures around a submarine  
773 pipeline buried in a trench layer with partially backfills. *Journal of Engineering  
774 Mechanics*, ASCE, 142, 04016042.

775 Zhao, H.-Y., Jeng, D.-S., Guo, Z., Zhang, J.S., 2014. Two-dimensional model for pore  
776 pressure accumulations in the vicinity of a buried pipeline. *Journal of Offshore  
777 Mechanics and Arctic Engineering*, ASME.136(4): 042001.  
778

779 Table 1 Wave characteristics and soil properties for WSSI model validation

Experiments	$H_w$ (m)	$T$ (s)	$h_w$ (m)	$D$ (m)	$e$ (m)	$G$ (N/m <sup>2</sup> )	$v$	$k_s$ (m/s)	$n_s$	$S_r$	$h_s$ (m)
Zang et al. (2010)	0.14 0.12	1.22 1.63	0.505 0.505	0.25 0.25	0 0	0 0	0 0	0 0	0 0	0 0	0 0
Liu et al. (2015)	3.5 3.5	9 9	5.2 5.2	0 0	0 0	$1.27 \times 10^7$ $1.27 \times 10^7$	0.3 0.3	$1.8 \times 10^{-4}$ $1.8 \times 10^{-4}$	0.425 0.425	0.996 0.951	1.8 1.8

780

781 Table 2 Parameters for studying wave-seabed-pile interaction

Wave characteristics			
Wave height, $H_w$ (m)	8.43	Wave period, $T$ (s)	13.6
Water depth, $h_w$ (m)	20	Wave length, $L_w$ (m)	188.5
$KC$ number	8.85		
Seabed characteristics			
Seabed thickness, $h_s$ (m)	38, 50, 62	Poisson's ratio, $\nu$	0.2
Submerged specific weight of sediment (kN/m <sup>3</sup> )	9.5	Permeability, $k_s$ (m/s)	$1 \times 10^{-4}$
Degree of saturation, $S_r$	0.98	Soil porosity, $n_s$	0.38
Young's modulus	See Section 4		
Mono-pile characteristics			
Diameter, $D$ (m)	6	Embedment depth, $e$ (m)	18, 30, 42
$D/L_w$	0.0032		

782

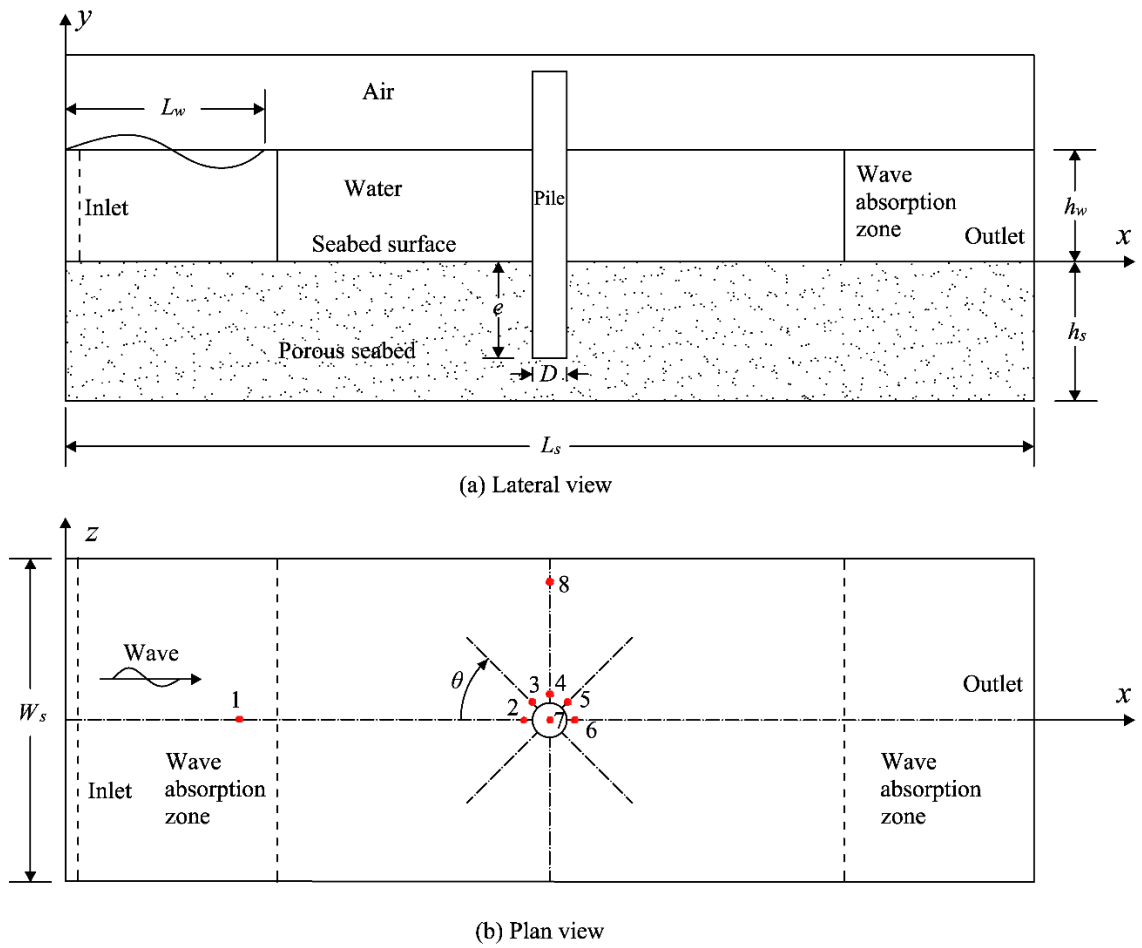


Figure 1 Sketch of the numerical wave tank. (a) Lateral view, (b) Plane view; the red dots in plan view are the locations of wave gauges or pressure sensors.

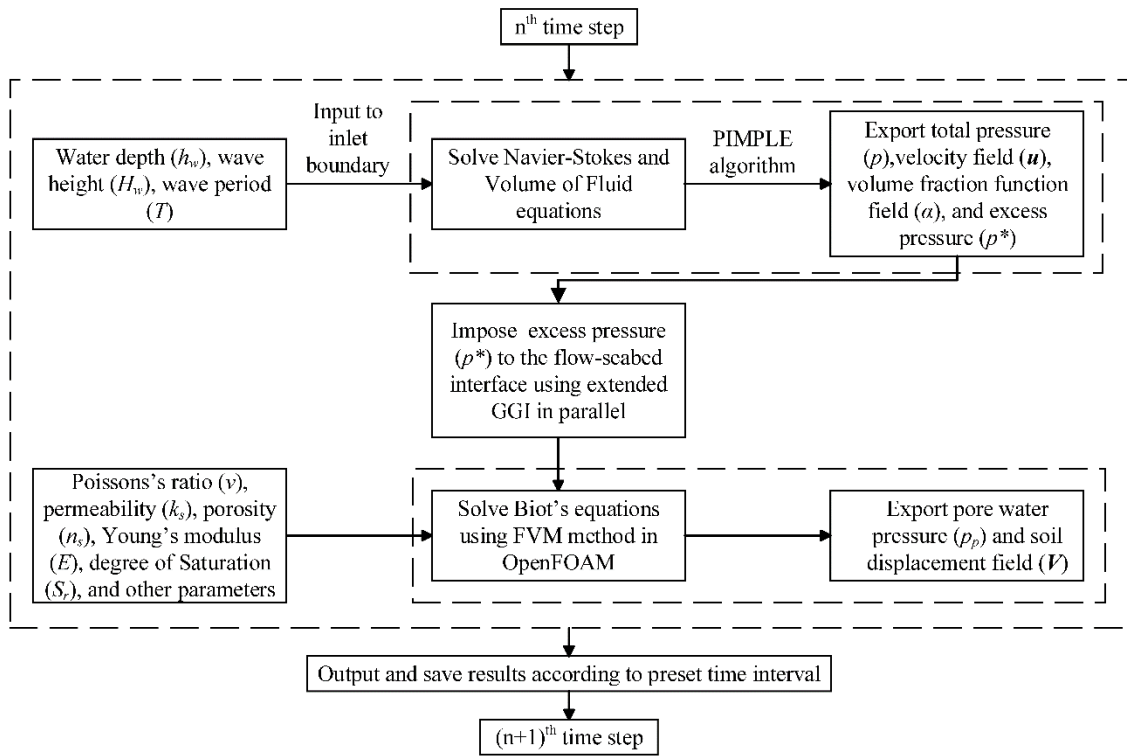


Figure 2 Coupled processes in the integrated WSSI model in OpenFOAM.



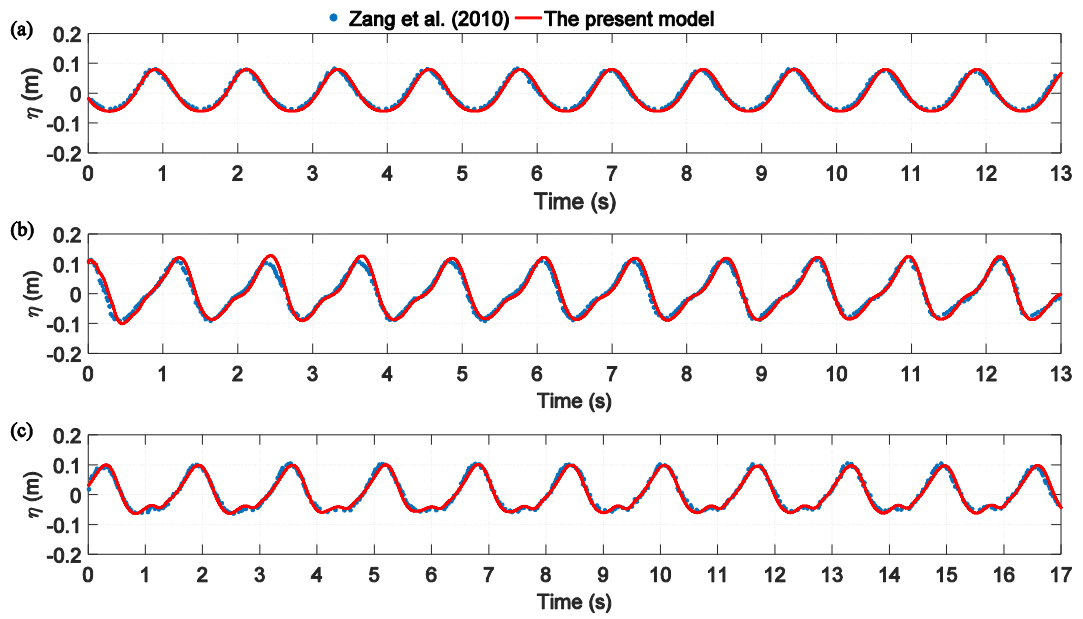


Figure 3 Validation of free surface elevation ( $\eta$ ) against experimental data (Zang et al., 2010). (a) Wave gauge 1 when  $H_w = 0.14\text{m}$  and  $T = 1.22\text{s}$ , (b) Wave gauge 2 when  $H_w = 0.14\text{m}$  and  $T = 1.22\text{s}$ , (c) Wave gauge 2 when  $H_w = 0.12\text{m}$  and  $T = 1.63\text{s}$ .

785

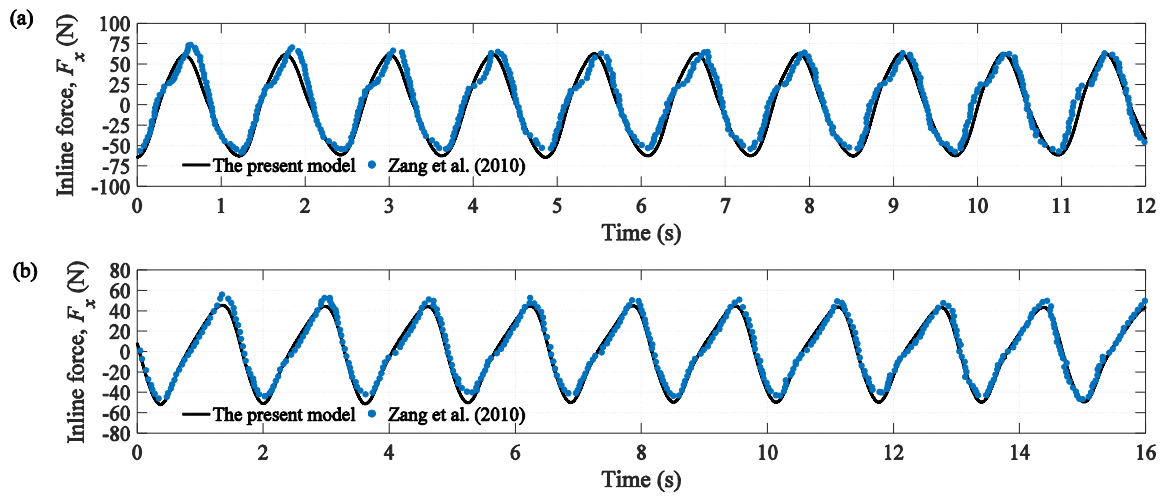


Figure 4 Comparison of inline force ( $F_x$ ) in OpenFOAM and experimental results (Zang et al., 2010). (a)  $H_w = 0.14\text{m}$  and  $T = 1.22\text{s}$ , (b)  $H_w = 0.12\text{m}$  and  $T = 1.63\text{s}$ .

786

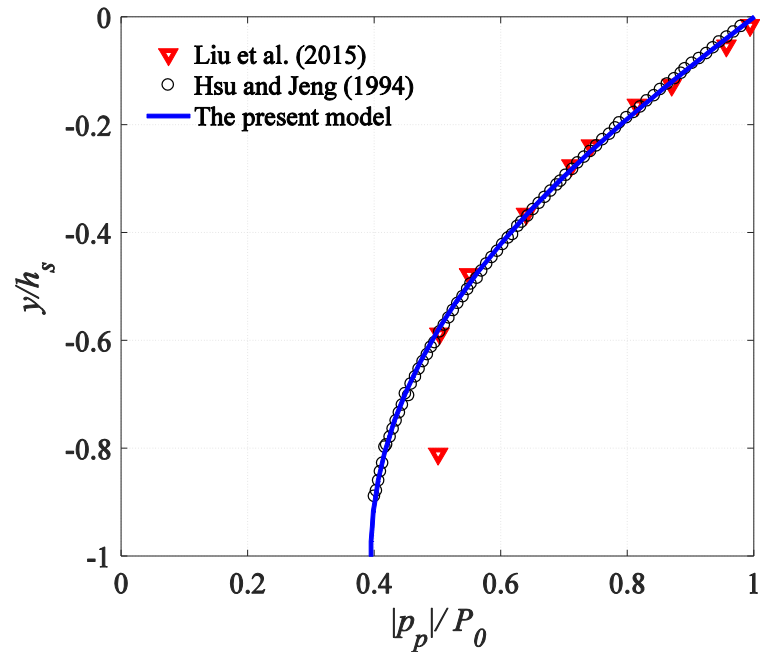


Figure 5 Comparison of vertical distribution of maximum pore water pressure between laboratory experiments from Liu et al. (2015) for  $S_r = 0.996$  and numerical reproduction in OpenFOAM.

787

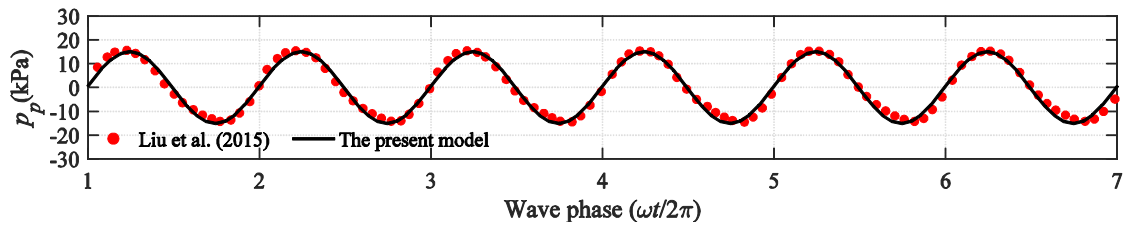


Figure 6 Comparison of wave-induced pore water pressure  $p_p$  between the experimental data for  $S_r = 0.951$  and numerical results in OpenFOAM at the depth  $y = -0.067\text{m}$  ( $y/h_s = -0.037$ ).

788

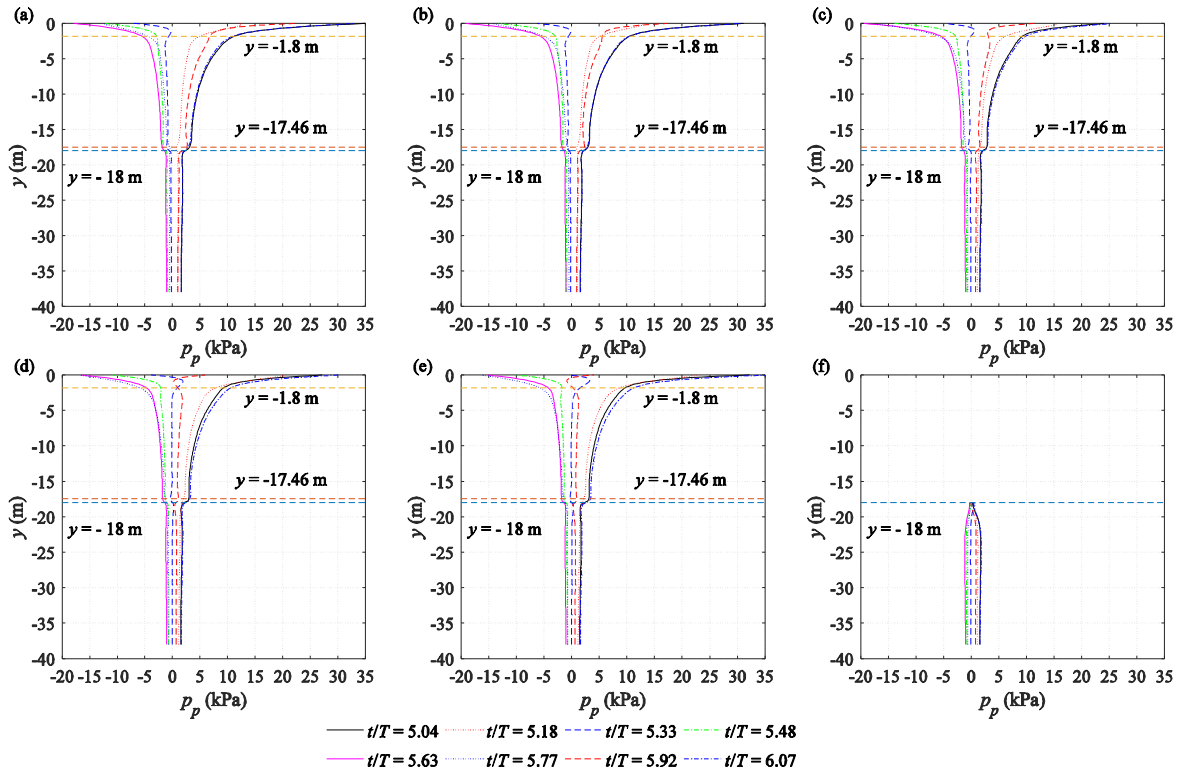


Figure 7 Vertical distribution of pore water pressure at various positions. (a)  $\theta = 0^\circ$ , (b)  $\theta = 45^\circ$ , (c)  $\theta = 90^\circ$ , (d)  $\theta = 135^\circ$ , (e)  $\theta = 180^\circ$ , (f) Centre of mono-pile bottom.

789

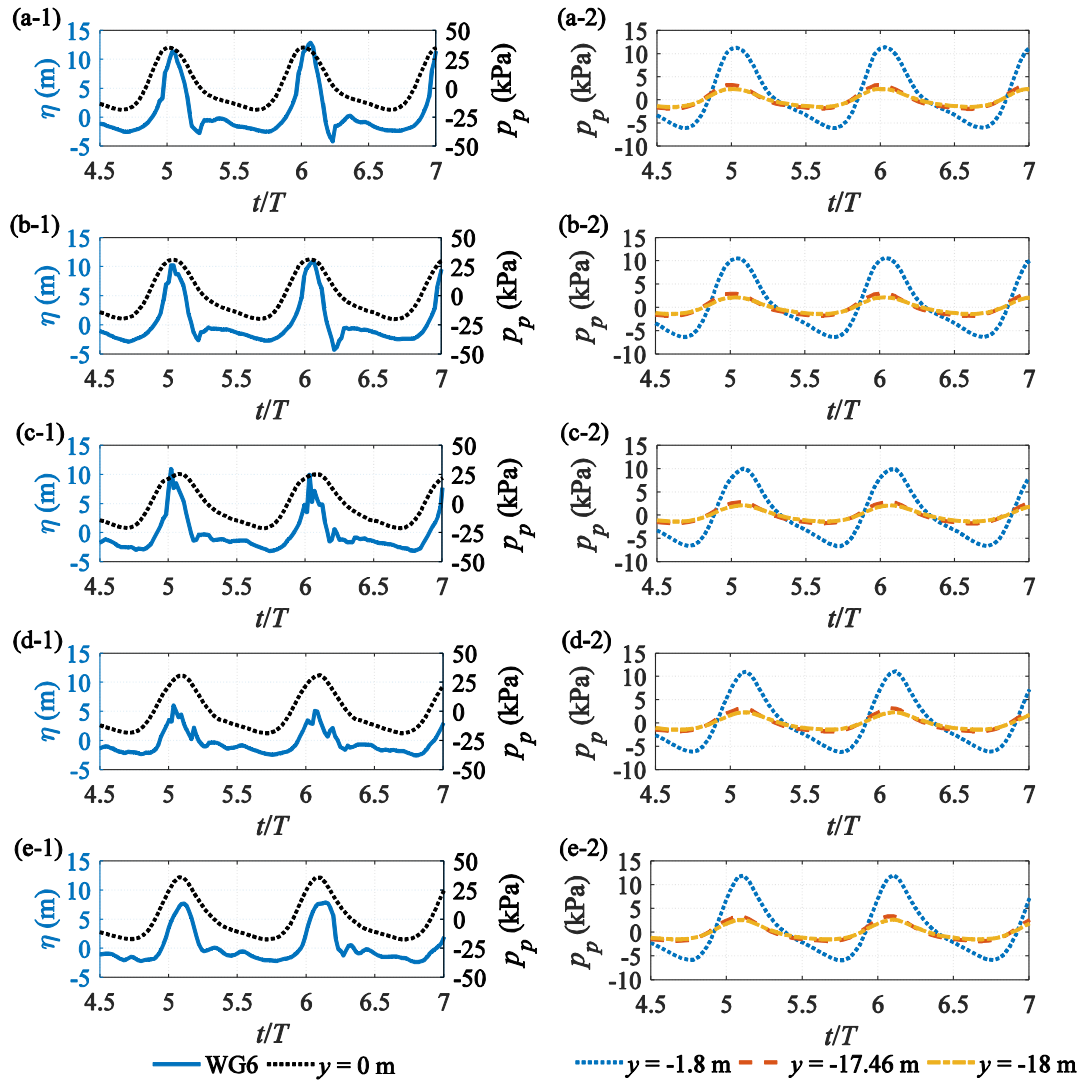


Figure 8 Time series of free surface elevation ( $\eta$ ) at various wave gauges. (a)  $\theta = 0^\circ$ , (b)  $\theta = 45^\circ$ , (c)  $\theta = 90^\circ$ , (d)  $\theta = 135^\circ$ , (e)  $\theta = 180^\circ$ . The first column are the comparisons of wave gauges and pore water pressure at  $y = 0\text{m}$ . The second column are the comparisons of pore water pressure at  $y = -3\text{m}$ ,  $y = -17.46\text{m}$ , and  $y = -18\text{m}$ , respectively.

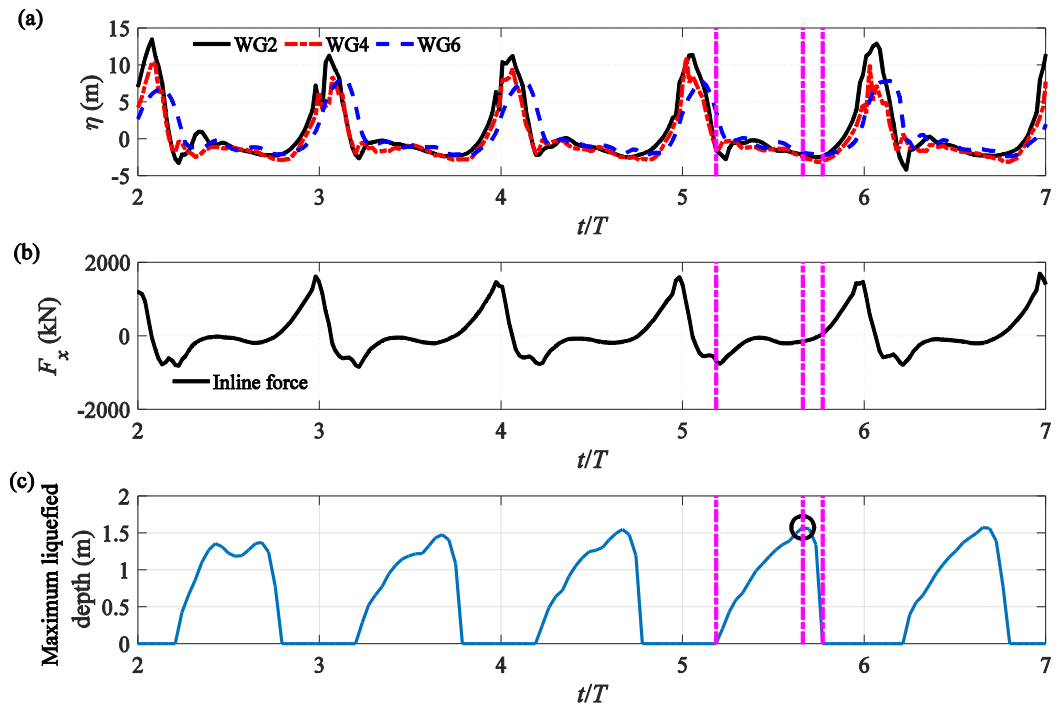


Figure 9 Time series of (a) free surface elevation ( $\eta$ ), (b) inline force, (c) maximum liquefied depth, with  $KC = 8.85$  and  $D/L_w = 0.032$ .

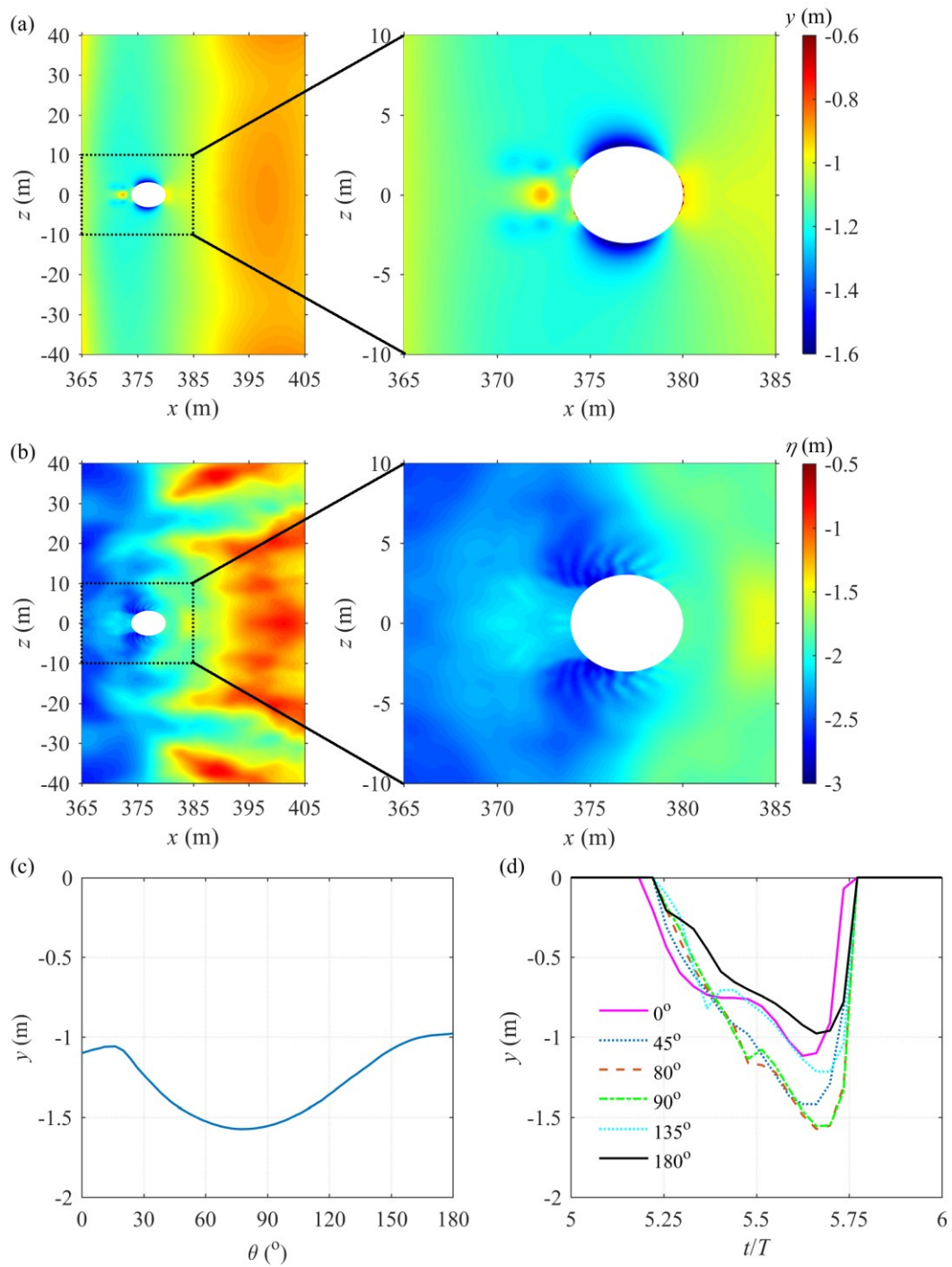


Figure 10 Liquefaction depth ( $y$ ) and free surface elevation ( $\eta$ ) around mono-pile foundation at  $t/T = 5.66$ . (a) Contour plot of liquefied depth, (b) Contour plot of free surface elevation ( $\eta$ ), (c) Liquefied depth for various  $\theta$ -locations at the soil-pile interface, (d) Time series of liquefied depth at various  $\theta$ -locations on the soil-pile interface.



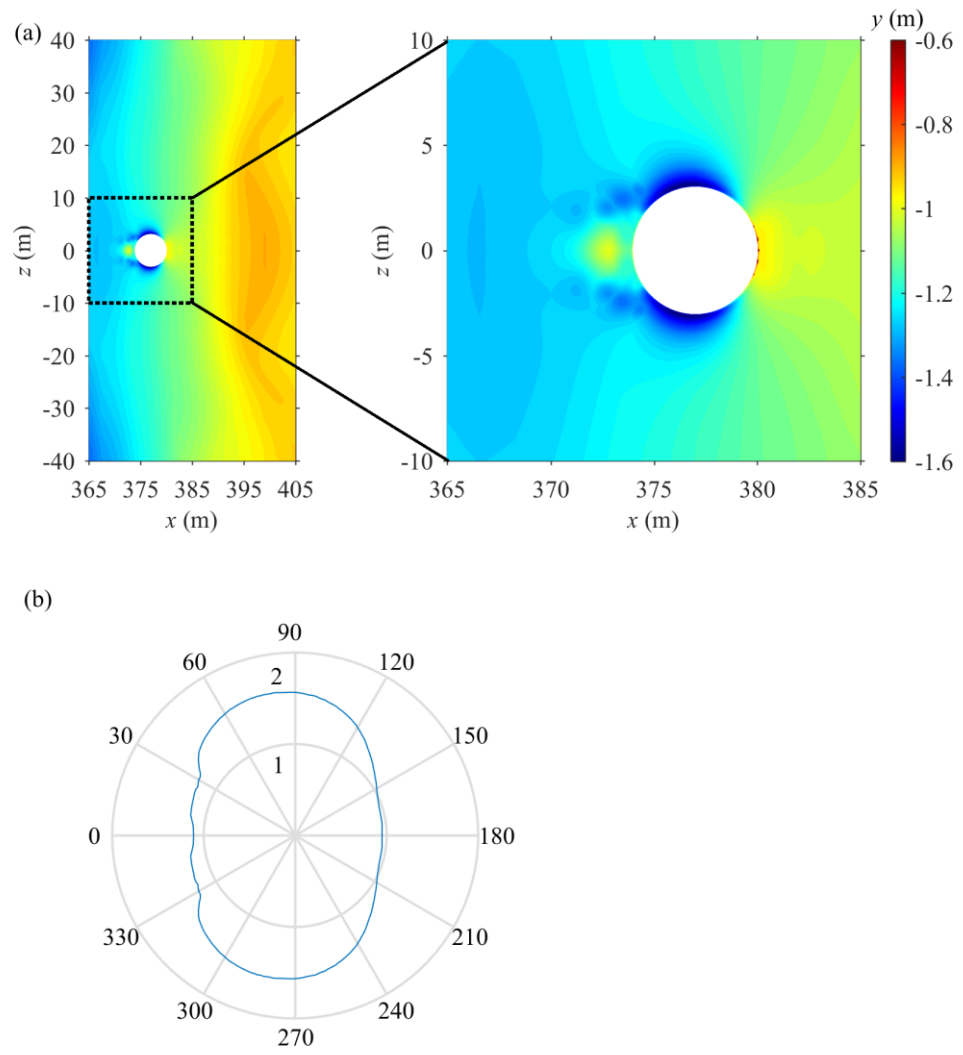


Figure 11 Maximum potential liquefaction depth over a wave period ( $t/T$  from 5 to 6). (a) Horizontal distribution, (b) Maximum liquefaction depth varying with  $\theta$  at the distance of 0.05m away from pile surface.

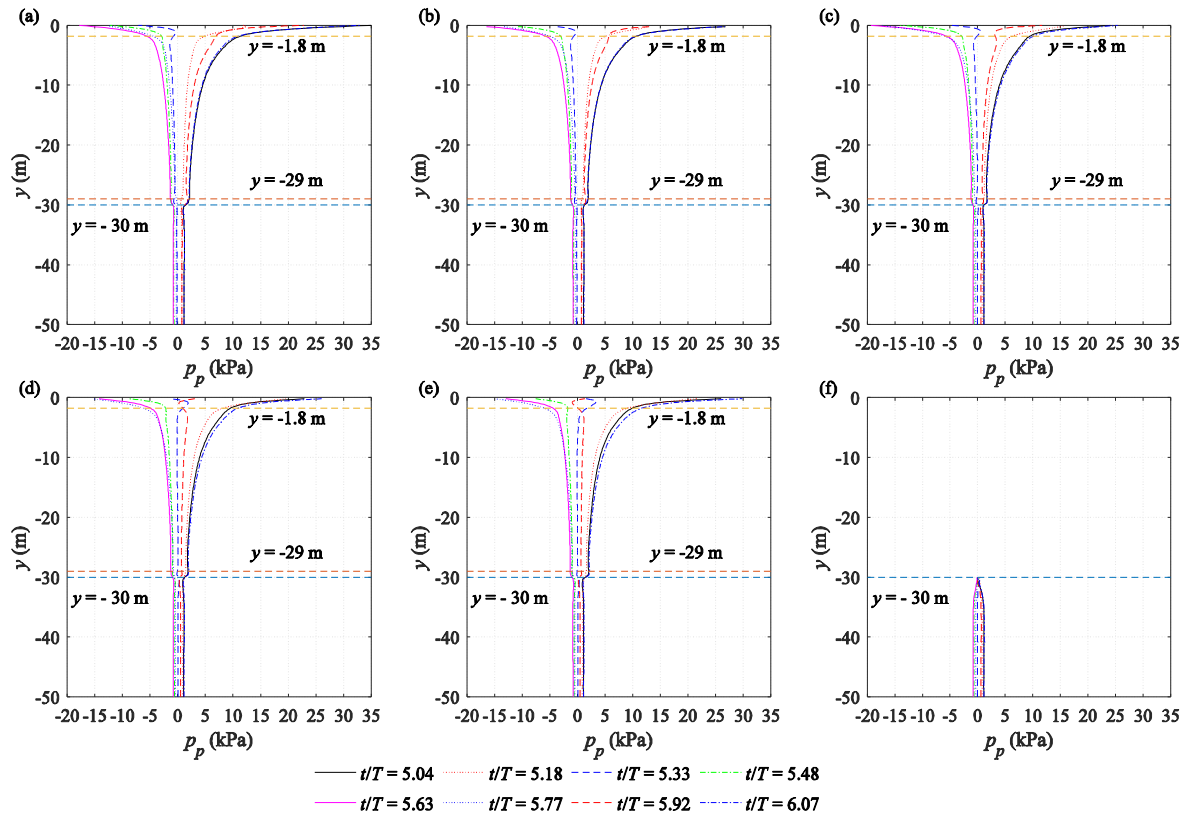


Figure 12 Vertical distribution of pore water pressure at various positions when embedment depth  $e = 30\text{m}$ . (a)  $\theta = 0^\circ$ , (b)  $\theta = 45^\circ$ , (c)  $\theta = 90^\circ$ , (d)  $\theta = 135^\circ$ , (e)  $\theta = 180^\circ$ , (f) Centre of mono-pile bottom.

794

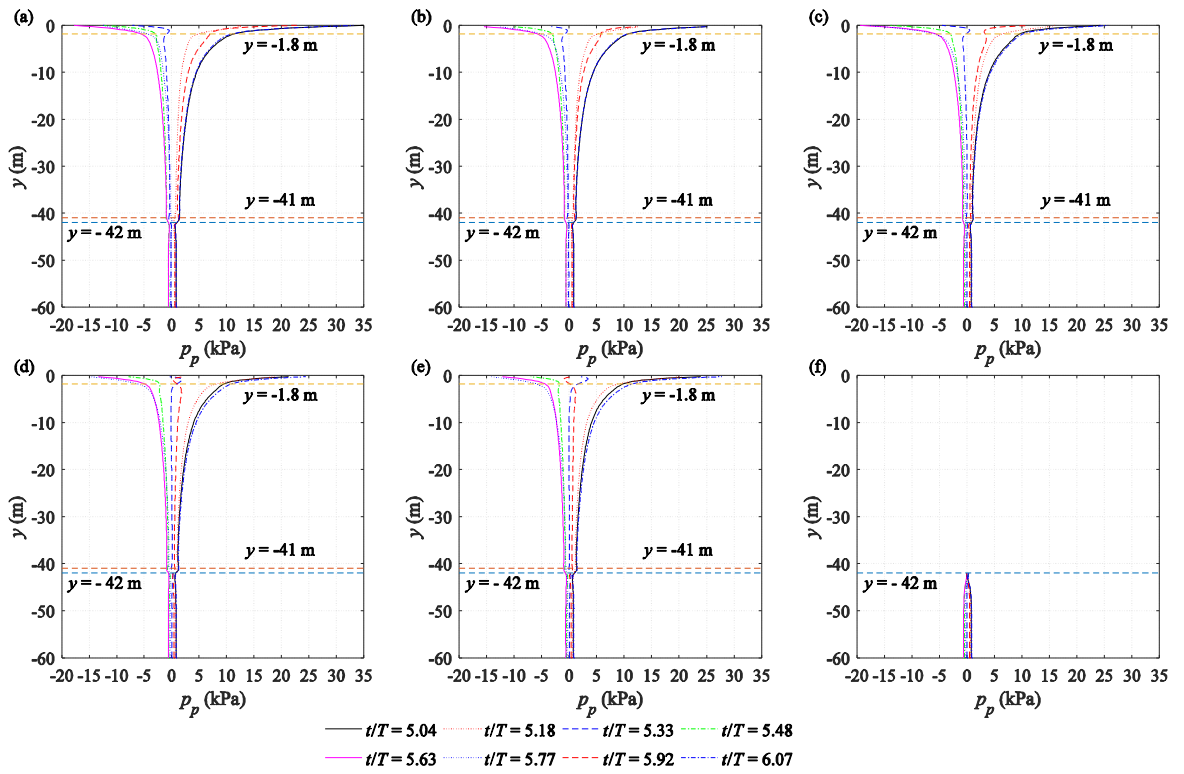


Figure 13 Vertical distribution of pore water pressure at various positions when embedment depth  $e = 42$  m. (a)  $\theta = 0^\circ$ , (b)  $\theta = 45^\circ$ , (c)  $\theta = 90^\circ$ , (d)  $\theta = 135^\circ$ , (e)  $\theta = 180^\circ$ , (f) Centre of mono-pile bottom.

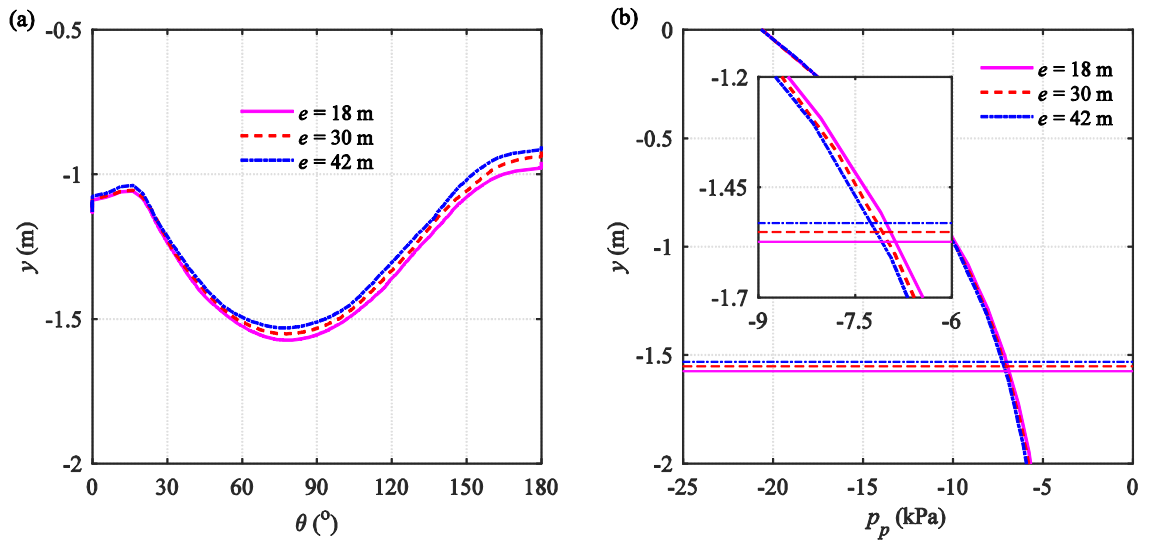


Figure 14 Comparison of liquefied depth with various embedment depths at  $t/T = 5.66$ . (a) Spatial description of liquefied depth varying with  $\theta$  on the soil-pile interface, (b) Liquefaction depth at  $\theta = 90^\circ$ , horizontal lines are maximum liquefaction depth.

796